SIAM J. APPL. MATH. © 2018 Society for Industrial and Applied Mathematics
Vol. 78, No. 3, pp. 1422–1449

DIFFERENTIAL FARADAY ROTATION AND POLARIMETRIC SAR*

MIKHAIL GILMAN† AND SEMYON TSYNKOV‡

Abstract. The propagation of linearly polarized electromagnetic waves through the Earth's ionosphere is accompanied by Faraday rotation (FR), which is due to gyrotropy of the ionospheric plasma in the magnetic field of the Earth. FR may cause distortions of the images taken by spaceborne polarimetric synthetic aperture radar (SAR). We show that the mechanism of those distortions is related to the variation of the FR angle within the bandwidth of the interrogating signals sent by the radar. This effect has not been analyzed previously in the context of SAR imaging. We also propose a special matched filter that we call the polarimetric matched filter (PMF). The PMF helps correct the FR-induced distortions and provides a provably superior SAR performance compared to the case of the traditional polarimetric SAR signal processing.

Key words. inverse scattering, scattering matrix, gyrotropy, electromagnetic waves, polarization, rotation of polarization plane, radar signal bandwidth, radar ambiguity theory, polarimetric matched filter, Earth's ionosphere, magnetic field of the Earth

AMS subject classifications. 35B20, 35R30, 45Q05, 78A35, 78A40, 78A45, 78A46, 78A55, 78A99, 78M35, 86A22, 86A25, 94A08, 94A12

DOI. 10.1137/17M114042X

1. Introduction.

Synthetic aperture radar (SAR) is an overhead imaging technology that uses microwave radio frequencies to obtain images of the surface of the Earth. The actual imaged quantity in SAR is referred to as the target reflectivity. In polarimetric SAR (PolSAR), the images are obtained in several scattering channels defined by the polarization of the incident and scattered (i.e., received) waves. In this way, PolSAR can help derive more than one characteristic of the imaged scene, as opposed to the case of the scalar (i.e., single-polarization) imaging. The additional information provided by PolSAR can be utilized in applications such as classification of the terrain and vegetation, soil moisture measurement, sea vessel detection, and ice thickness measurement; see [14, 17, 22].

When the SAR antenna is mounted on a satellite (spaceborne SAR), the signals it emits travel through the ionosphere on their way back and forth between the antenna and the target. The ionospheric plasma distorts the propagating radar signals. The distortions decrease as the carrier frequency of the radar increases, and for many current spaceborne SAR systems they appear insignificant. However, certain tasks, such as foliage and ground penetration, benefit from longer wavelengths (i.e., lower frequencies). Therefore, in a number of contemplated spaceborne SAR missions, the system parameters have to be chosen such that the ionospheric distortions appear quite substantial [13, 21]. In our prior work [10, Chapter 3], we have proposed to mitigate those distortions with the help of dual carrier probing. Other relevant publications in the literature include [16, 2, 19, 1, 15].

*Received by the editors July 25, 2017; accepted for publication (in revised form) February 26, 2018; published electronically May 15, 2018.
http://www.siam.org/journals/siap/78-3/M114042.html
Funding: This work was supported by the U.S. Air Force Office of Scientific Research (AFOSR) under awards FA9550-14-1-0218 and FA9550-17-1-0230.
†Corresponding author. Department of Mathematics, North Carolina State University, Raleigh, NC 27695 (mgilman@ncsu.edu, http://www4.ncsu.edu/~mgilman/).
‡Department of Mathematics, North Carolina State University, Raleigh, NC 27695 (tsynkov@math.ncsu.edu, http://www4.ncsu.edu/~stsynkov/).

One particular effect of transionospheric propagation, called the Faraday rotation (FR), is especially important in the context of PolSAR because it is the effect of rotation of the polarization plane of the emitted and scattered signals. This effect is due to gyrotropy of the ionospheric plasma in the external magnetic field (the magnetic field of the Earth). When the complete polarization information is available (the so-called quad-pol imaging) and the FR angle is known, the effect of FR on SAR can be mitigated by means of a simple linear transformation applied to the four imaging channels, as described, e.g., in [7]. However, this approach assumes that every part of the signal is rotated by the same angle. Yet the FR angle is a function of the propagating frequency, and typical SAR signals have a certain bandwidth. Hence, different frequency components of the signal will be rotated by different angles; this effect will be called the differential Faraday rotation (dFR). In the case of linear frequency modulated (LFM) signals, the instantaneous frequency of a signal is a linear function of time; hence, a linearly polarized LFM signal becomes twisted as it propagates through a magnetized plasma. As the variation of the FR angle for a given signal approaches π, the polarization information gets compromised, and the aforementioned traditional image-based correction procedure becomes inadequate.

In this work, we introduce the concept of a polarimetric matched filter (PMF), which is a quad-pol signal processing formulation that addresses the aforementioned twisting effect. The main novelty of the PMF is that it takes into account all polarization channels at the signal processing stage, whereas in the traditional polarimetric technique, the compensation of FR is done as postprocessing of the images in individual channels. We show that, unlike the traditional approach, the PMF can essentially eliminate the distortions due to dFR. We also analyze the performance of the traditional (i.e., image-based) correction procedure and derive the expressions for the resulting polarimetric error. The dFR effect on single-polarization SAR has been analyzed in [10, Chapter 5]. Note that coupled processing of polarization channels has been introduced as a means of extracting the polarimetric target information from isotropic clutter [23]. Including FR into the SAR processor has also been proposed in [24], although not in the context of dFR.

Section 2 provides the necessary background information used throughout this work. Section 3 presents the analysis of dFR and its effect on radar imaging in the simplified single-pulse framework. The full-fledged SAR geometry is considered in section 4. In section 5, we show how our analysis of dFR appears relevant for certain SAR applications. In doing so, we use the parameters of a hypothetical P-band spaceborne SAR system that is strongly affected by transionospheric propagation; see Table 1. For comparison, we also use in section 5 the parameters of the future BIOMASS mission as presented in [13]. Table 2 provides the list of acronyms used in this work.

Executive summary. The FR angle φ_{F} is assumed to be given by formula (2), where all the quantities are known. When the transmitted waveform is a linearly polarized chirp as given by (11), (12), then the measure of distortions of the traditional polarimetric imaging is given by (94), (91) and illustrated in Figure 2. In order to reduce those distortions, the image should be formed according to (84), where the data matrix $\mathbf{M}$ is given by (8), A and χ are given by (12), $\mathfrak{t}_{\mathrm{gr}}$ is introduced by (18), and $\mathbf{R}$ is given by (3).

2. FR of a monochromatic wave scattered by a point target. We will introduce the fundamentals of our discussion using the basic example of a monochromatic linearly polarized electromagnetic wave that propagates through a homogeneous

Table 1
Typical values of the ionospheric and SAR system parameters.

Parameter	Notation	Value	Reference
Magnitude of geomagnetic field	$\|\boldsymbol{H}_0\|$	$0.5\,Gauss$	(2)
Typical plasma electron frequency in the ionosphere	$\frac{\omega_{\rm pe}}{2\pi}$	$9\,MHz$	(2)
Radar carrier frequency	$\frac{\omega_0}{2\pi}$	$300\,MHz$	(11)
Pulse (chirp) duration	τ	$5\cdot 10^{-5}s$	(12)
Bandwidth	$\frac{B}{2\pi}$	$8\,MHz$	(13)
One-way distance from the antenna to the target	$\|x\|$, R	$1000\,km$	(38)
Total electron content in the ionosphere	N_H	$5\cdot 10^{13}cm^{-2}$	(78)
Look angle	θ	60°	(79)
Length of synthetic aperture	$L_{\rm SA}$	$50\,km$	(77)

Table 2
List of acronyms.

Acronym	Meaning	Reference
SAR	synthetic aperture radar	—
PolSAR	polarimetric SAR	—
PolInSAR	polarimetric SAR interferometry	section 5
FR	Faraday rotation	(3)
dFR	differential Faraday rotation	(15), (19)
TEC	total electron content	(78)
PSF	point spread function	(29), (36), (48)
PMF	polarimetric matched filter	(25)
ISLR	integrated sidelobe ratio	(57), (58)
PPCM	point-based polarimetric contamination metric	(61)
APCM	area-based polarimetric contamination metric	(64)

plasma and is scattered by a point target. The time dependence for the wave field is $\propto e^{-i\omega t}$, where the frequency ω is considered constant throughout this section. The point source (antenna) is located at $\boldsymbol{x}$, and the scatterer is located at $\boldsymbol{z}$. We assume that the scatterer reflects the electromagnetic waves in all polarimetric channels. Let $\mathbf{e}_{\rm H}$ and $\mathbf{e}_{\rm V}$ be two unit vectors orthogonal to each other and to the direction of propagation:[1] $(\mathbf{e}_{\rm H},\mathbf{e}_{\rm V})=0$, $\mathbf{e}_{\rm V}\times\mathbf{e}_{\rm H}=\frac{\boldsymbol{z}-\boldsymbol{x}}{|\boldsymbol{z}-\boldsymbol{x}|}$. These unit vectors will denote the horizontal and vertical linear polarization, respectively. For an incident electromagnetic wave emitted by the antenna, the electric field $\boldsymbol{E}^{\rm i}$ is orthogonal to the propagation direction. Therefore, it can be thought of as a vector with two components: $E^{\rm i}_{\rm H}=(\mathbf{e}_{\rm H},\boldsymbol{E}^{\rm i})$ and $E^{\rm i}_{\rm V}=(\mathbf{e}_{\rm V},\boldsymbol{E}^{\rm i})$, where $(\cdot,\cdot)$ denotes the dot product of three-dimensional vectors. The propagation with no FR is given by

$$\begin{pmatrix}E^{\rm i}_{\rm H}\\E^{\rm i}_{\rm V}\end{pmatrix}(t,\boldsymbol{z})=Ke^{i\omega R_{\boldsymbol{z}}/v_{\rm ph}}\begin{pmatrix}E^{\rm i}_{\rm H}\\E^{\rm i}_{\rm V}\end{pmatrix}(t,\boldsymbol{x}), \tag{1}$$

where $R_{\boldsymbol{z}}=|\boldsymbol{z}-\boldsymbol{x}|$ is the distance between the antenna and the target, $v_{\rm ph}$ is the phase velocity of electromagnetic waves in the ionospheric plasma,[2] and K is a scalar

[1] For the given $\boldsymbol{z}$ and $\boldsymbol{x}$, these conditions define the vectors $\mathbf{e}_{\rm H}$ and $\mathbf{e}_{\rm V}$ up to a common rotation about $\boldsymbol{z}-\boldsymbol{x}$. If the target is a point scatterer, it is not necessary to specify these vectors any further. Otherwise, when we have a distributed scatterer (planar or mostly planar) as in section 4, and $\boldsymbol{z}-\boldsymbol{x}$ is not necessarily orthogonal to the corresponding plane, then $\mathbf{e}_{\rm H}$ should be chosen parallel to the plane and $\mathbf{e}_{\rm V}$ pointing from the source $\boldsymbol{x}$ toward the plane, as explained in [3, section 2.1].

[2] In a homogeneous ionosphere, $v_{\rm ph}$ is a constant that slightly exceeds the speed of light c; see (17).

that accounts for the possible signal attenuation.[3]

The FR is a manifestation of double circular refraction. A linearly polarized wave impinging on a layer of anisotropic material (e.g., gyrotropic plasma) can be represented as the sum of two circularly polarized (helical) waves with opposite directions of polarization. In the material, the latter will propagate with slightly different phase speeds. This difference translates into a slow rotation of the polarization plane of the original linearly polarized wave. In the case of a cold magnetized plasma, the FR angle φ_{F} is given by (see, e.g., [20, 11])

$$\varphi_{\mathrm{F}} = -\frac{R_{\boldsymbol{z}}}{2c}\frac{\omega_{\mathrm{pe}}^2 \Omega_{\mathrm{e}} \cos\beta}{\omega^2}, \quad \text{where} \quad \omega_{\mathrm{pe}}^2 = \frac{4\pi N_{\mathrm{e}} e^2}{m_{\mathrm{e}}}, \quad \Omega_{\mathrm{e}} = -\frac{e|\boldsymbol{H}_0|}{m_{\mathrm{e}} c}. \tag{2}$$

In (2), ω_{pe} and Ω_{e} are the electron plasma frequency and gyrofrequency, respectively, m_{e} and $-e$ are the mass and charge of the electron, N_{e} denotes the electron number density in the ionosphere, and $\boldsymbol{H}_0$ is the magnetic field of the Earth. The quantity β in formula (2) is the angle between the direction $\boldsymbol{z} - \boldsymbol{x}$ and $\boldsymbol{H}_0$. We see that φ_{F} is a function of $\boldsymbol{z}$, but as long as we consider a given point target and a continuous wave with a fixed frequency ω, the FR angle φ_{F} can be thought of as a constant. Until section 4, we will also be assuming that ω_{pe}, Ω_{e}, and β are constant.

When the wave propagates along the external magnetic field, the direction of FR in plasma is clockwise if looking down the propagation direction; otherwise, it is counterclockwise. To describe the evolution of the electric field in space, we introduce the rotation matrix $\mathbf{R} = \mathbf{R}(\varphi_{\mathrm{F}})$ as follows (see, e.g., [7]):

$$\mathbf{R}(\varphi_{\mathrm{F}}) \stackrel{\mathrm{def}}{=} \begin{pmatrix} \cos\varphi_{\mathrm{F}} & \sin\varphi_{\mathrm{F}} \\ -\sin\varphi_{\mathrm{F}} & \cos\varphi_{\mathrm{F}} \end{pmatrix}, \tag{3}$$

such that

$$\begin{pmatrix} E_{\mathrm{H}}^{\mathrm{i}} \\ E_{\mathrm{V}}^{\mathrm{i}} \end{pmatrix}(t, \boldsymbol{z}) = K e^{i\omega R_z / v_{\mathrm{ph}}} \mathbf{R}(\varphi_{\mathrm{F}}) \cdot \begin{pmatrix} E_{\mathrm{H}}^{\mathrm{i}} \\ E_{\mathrm{V}}^{\mathrm{i}} \end{pmatrix}(t, \boldsymbol{x}) \tag{4}$$

(cf. formula (1)). If the propagation is oblique yet not normal to the magnetic field (technically, if $\left|\frac{\Omega_{\mathrm{e}}}{2\omega}\right| \ll |\cos\beta| < 1$), then one can observe the additional small variations of the complex field amplitude with distance. The reason for their appearance is the elliptical (rather than circular) polarization of obliquely propagating helical waves. However, the ratio of semiaxes of the corresponding polarization ellipses differs from one by only about $\left|\frac{\Omega_{\mathrm{e}} \sin^2\beta}{2\omega\cos\beta}\right|$ (see, e.g., [11, section 11]). For the systems that we are considering the value of $\left|\frac{\Omega_{\mathrm{e}}}{\omega}\right| \approx 5 \cdot 10^{-3}$ is small; see Table 1. Therefore, the aforementioned amplitude variations can be ignored, and formula (4) can be used the way it is.

Scattering by a point target (located at $\boldsymbol{z}$) is described by the matrix $\mathbf{S}$ that relates the horizontal and vertical components of the incident field $\boldsymbol{E}^{\mathrm{i}}$ and scattered field $\boldsymbol{E}^{\mathrm{s}}$. We will be using the following indexing convention:[4]

$$\begin{pmatrix} E_{\mathrm{H}}^{\mathrm{s}} \\ E_{\mathrm{V}}^{\mathrm{s}} \end{pmatrix}(t, \boldsymbol{z}) = \begin{pmatrix} S_{\mathrm{HH}} & S_{\mathrm{HV}} \\ S_{\mathrm{VH}} & S_{\mathrm{VV}} \end{pmatrix} \cdot \begin{pmatrix} E_{\mathrm{H}}^{\mathrm{i}} \\ E_{\mathrm{V}}^{\mathrm{i}} \end{pmatrix}(t, \boldsymbol{z}). \tag{5}$$

[3] The field amplitude at the point source is singular. This well-known fact is not important for our subsequent discussion. The attenuation factor K will be disregarded after (9).

[4] A different indexing convention is used, e.g., in [7].

The propagation of the scattered field from $\boldsymbol{z}$ back to $\boldsymbol{x}$ can be described using the same frame of reference that involves the vectors $\mathbf{e}_\mathrm{H}$ and $\mathbf{e}_\mathrm{V}$; this approach is called the backward scattering alignment; see [3, section 2.1] and [7] for details. Then, similarly to (4), we have

$$\begin{pmatrix} E^\mathrm{s}_\mathrm{H} \\ E^\mathrm{s}_\mathrm{V} \end{pmatrix}(t,\boldsymbol{x}) = K^2 e^{2i\omega R_z/v_\mathrm{ph}} \mathbf{R}(\varphi_\mathrm{F}) \cdot \mathbf{S} \cdot \mathbf{R}(\varphi_\mathrm{F}) \cdot \begin{pmatrix} E^\mathrm{i}_\mathrm{H} \\ E^\mathrm{i}_\mathrm{V} \end{pmatrix}(t,\boldsymbol{x}). \tag{6}$$

We see that for the two-way propagation, the FR angle doubles rather than cancels.

Suppose that the antenna emits two monochromatic signals of equal amplitude E_0 in two basic linear polarizations, horizontal (H) and vertical (V):

$$\begin{pmatrix} E^\mathrm{i}_\mathrm{H} \\ E^\mathrm{i}_\mathrm{V} \end{pmatrix}_{(\mathrm{H},\mathrm{V})}(t,\boldsymbol{x}) = \boldsymbol{E}_{(\mathrm{H},\mathrm{V})} e^{-i\omega t}, \quad \text{where} \quad \boldsymbol{E}_{(\mathrm{H})} \stackrel{\mathrm{def}}{=} \begin{pmatrix} E_0 \\ 0 \end{pmatrix}, \quad \boldsymbol{E}_{(\mathrm{V})} \stackrel{\mathrm{def}}{=} \begin{pmatrix} 0 \\ E_0 \end{pmatrix}. \tag{7}$$

Denote the received data (i.e., the scaled reflected fields at $\boldsymbol{x}$) as follows:

$$\begin{pmatrix} M_\mathrm{HH} \\ M_\mathrm{VH} \end{pmatrix}(t) \stackrel{\mathrm{def}}{=} \frac{1}{K^2E_0} \begin{pmatrix} E^\mathrm{s}_\mathrm{H} \\ E^\mathrm{s}_\mathrm{V} \end{pmatrix}_{(\mathrm{H})}(t,\boldsymbol{x}) \ \text{ and } \ \begin{pmatrix} M_\mathrm{HV} \\ M_\mathrm{VV} \end{pmatrix}(t) \stackrel{\mathrm{def}}{=} \frac{1}{K^2E_0} \begin{pmatrix} E^\mathrm{s}_\mathrm{H} \\ E^\mathrm{s}_\mathrm{V} \end{pmatrix}_{(\mathrm{V})}(t,\boldsymbol{x}), \tag{8}$$

where the vector $(E^\mathrm{s}_\mathrm{H}, E^\mathrm{s}_\mathrm{V})^\mathrm{T}$ for each polarization is given by (6). Then, the data matrix $\mathbf{M}(t)$ is related to the scattering matrix $\mathbf{S}$ by

$$\mathbf{M}(t) = e^{-i\omega(t-2R_z/v_\mathrm{ph})} \mathbf{R}(\varphi_\mathrm{F}) \cdot \mathbf{S} \cdot \mathbf{R}(\varphi_\mathrm{F}). \tag{9}$$

Note that the scalar K^{-2} could have been incorporated into the scattering matrix $\mathbf{S}$ rather than into the definition of $\mathbf{M}$, thereby resolving the issue of the dependence of attenuation on the propagation distance (i.e., on $\boldsymbol{z}$) when $\mathbf{S}$ becomes a function of $\boldsymbol{z}$; see (24) in section 3.1. From here on, this scalar will be disregarded.

Equation (3) implies, in particular, that $\mathbf{R}(\varphi_1 + \varphi_2) = \mathbf{R}(\varphi_1) \cdot \mathbf{R}(\varphi_2)$. Using this property, one can reconstruct the scattering matrix of a point scatterer from the data (9) as follows:

$$\mathbf{S} = e^{i\omega(t-2R_z/v_\mathrm{ph})} \mathbf{R}(-\varphi_\mathrm{F}) \cdot \mathbf{M}(t) \cdot \mathbf{R}(-\varphi_\mathrm{F}). \tag{10}$$

As $\mathbf{M}(t) \propto e^{-i\omega t}$ (see (7)–(9)), formula (10) yields $\mathbf{S}$ that is independent of t, as expected. It is worth noting that the reconstruction formula (10) remains valid regardless of the value of the FR angle, including those cases where the received field is orthogonal or nearly orthogonal to the emitted field, i.e., $\varphi_\mathrm{F} \approx \frac{\pi n}{2} + \frac{\pi}{4}$, $n \in \mathbb{Z}$.

As far as the potential applications are concerned, formula (10) represents an idealized situation: a point scatterer at a known distance from the antenna. Besides the distance $R_{\boldsymbol{z}}$, the signal processing procedure $\mathbf{M} \longrightarrow \mathbf{S}$ requires knowledge of the parameters of the propagation medium, in particular, the electron plasma frequency ω_pe and the magnetic field of the Earth $\boldsymbol{H}_0$. In transionospheric SAR imaging, these parameters can be estimated from the measurements of the total electron content (TEC; see definition (78) in section 4) combined with geomagnetic data [10]. Hereinafter, we assume that these parameters are available.

3. Single-pulse imaging. In this section, we introduce the polarimetric matched filter (PMF) in a simplified setting where the target is probed by just one radar pulse. This setting allows us to analyze, with few exceptions, the effect of FR on SAR without having to address the complications due to the three-dimensional geometry. (The latter will be considered in section 4.) In particular, for a single probing signal, the imaged area can be represented by an interval of a straight line, and the antenna can be located on the same line. This line, which we also take as the coordinate axis, is assumed parallel to the external magnetic field so that $\cos\beta = 1$ in formula (2). In doing so, we place the origin in the target area and denote the scalar coordinates of the antenna, image, and target by x, y, and z, respectively. The direction of the axis is taken from the antenna to the target, so $x < y$ and $x < z$.

To probe the target, we will emit a single pulse in each of the two basic linear polarizations from the location $x = \text{const}$ and process the returns received in two polarizations as well. This yields a one-dimensional polarimetric image. In SAR terms, it corresponds to quad-pol signal processing in fast time only. For simplicity, the propagation medium, i.e., the ionosphere, is still considered homogeneous in this section. Moreover, the plasma electron frequency and the gyrofrequency (see formula (2)) needed for the construction and application of the PMF are assumed known. A nonhomogeneous medium, as well as a realistic three-dimensional geometry that requires a sequence of pulses emitted from different antenna locations (i.e., a full-fledged SAR), will be considered in section 4.

3.1. PMF. Instead of the monochromatic waves (7), the radar emits narrow-band interrogating pulses. The most commonly used are linear frequency modulated (LFM) pulses, also known as chirps:

$$\begin{pmatrix} E^{\mathrm{i}}_{\mathrm{H}} \\ E^{\mathrm{i}}_{\mathrm{V}} \end{pmatrix}_{(\mathrm{H,V})} (t, x) = \boldsymbol{E}_{(\mathrm{H,V})} A(t) e^{-i\omega_0 t}, \tag{11}$$

where

$$A(t) = \chi_\tau(t) e^{-i\alpha t^2}, \quad \chi_\tau(t) = \begin{cases} 1, & t \in [-\tau/2, \tau/2], \\ 0 & \text{otherwise}. \end{cases} \tag{12}$$

In (11), ω_0 is the carrier frequency, α is the chirp rate, and χ_τ is the indicator function for a pulse of duration τ. One can derive the expression for the instantaneous frequency by differentiating (11) with respect to t inside the support of $A(t)$:

$$\omega(t) = \omega_0 + 2\alpha t = \omega_0 + \frac{B}{\tau} t, \quad |t| \leqslant \frac{\tau}{2}, \tag{13}$$

where $B = 2\alpha\tau > 0$ is the chirp bandwidth.[5] For a narrowband signal, we have $B \ll \omega_0$.

It is known that when a narrowband pulse propagates through a dispersive medium, the pulse envelope moves with the group velocity, while the carrier oscillation propagates with the phase velocity. The expression for the pulse waveform can be obtained by Fourier transforming the initial waveform, propagating each individual harmonic with the corresponding phase velocity, and then applying the inverse Fourier transform [10, section 3.2]. For the case of a magnetized plasma, the FR should also be taken into account. The propagation of LFM signals through a magnetized plasma was considered in [9] and [10, section 5.2]. In this case, the propagation formula (4) is replaced with

$$\begin{pmatrix} E^{\mathrm{i}}_{\mathrm{H}} \\ E^{\mathrm{i}}_{\mathrm{V}} \end{pmatrix}_{(\mathrm{H,V})} (t, z) = A_\delta(t - R_z/v_{\mathrm{gr}}(\omega_0)) e^{-i\omega_0(t - R_z/v_{\mathrm{ph}}(\omega_0))} \mathbf{R}(\breve{\varphi}_{\mathrm{F}}) \cdot \boldsymbol{E}_{(\mathrm{H,V})}, \tag{14}$$

[5]The quantity B in (13) is the bandwidth expressed in radians per second. In Table 1, the bandwidth $B/2\pi$ is given in *Hz*.

where $\boldsymbol{E}_{(\mathrm{H})}$ and $\boldsymbol{E}_{(\mathrm{V})}$ are introduced in (7), while the attenuation coefficient K has been dropped per the discussion right after (9). The structure of the matrix $\mathbf{R}(\breve{\varphi}_{\mathrm{F}})$ in (14) is given by (3) with

$$\breve{\varphi}_{\mathrm{F}} = -\frac{R_z}{2c}\frac{\omega_{\mathrm{pe}}^2\Omega_{\mathrm{e}}}{\omega^2(t - R_z/v_{\mathrm{gr}}(\omega_0))}. \tag{15}$$

A_δ in (14) represents a new scalar pulse envelope with the modified chirp rate and duration (see also [10, section 3.2]):

$$A_\delta(t) = \chi_{\tau-\delta\tau}(t)e^{-i(\alpha+\delta\alpha)t^2}, \quad \delta\tau = \frac{B}{\omega_0}\frac{R_z}{c}\frac{\omega_{\mathrm{pe}}^2}{\omega_0^2}, \quad \delta\alpha = \alpha\frac{\delta\tau}{\tau}, \tag{16}$$

where $R_z = |z - x| \equiv z - x$, and $v_{\mathrm{ph,gr}}$ denote the phase and group velocities in plasma, respectively:

$$v_{\mathrm{ph}} = \sqrt{\omega_{\mathrm{pe}}^2 + k^2c^2}/k, \quad v_{\mathrm{gr}} = kc^2/\sqrt{\omega_{\mathrm{pe}}^2 + k^2c^2}. \tag{17}$$

The quantity k in formulae (17) is the wavenumber (see, e.g., [11]): $k \equiv k(\omega) = \sqrt{\omega^2 - \omega_{\mathrm{pe}}^2}/c = 2\pi/\lambda$. Note that the expressions for v_{ph} and v_{gr} contain no terms associated with the external magnetic field. As shown in [10, section 5.1], one can use these simplified phase and group velocities because for the typical ionospheric and radar parameters of interest (see Table 1) we have $\omega_{\mathrm{pe}} \ll \omega_0$ and $|\Omega_{\mathrm{e}}| \ll \omega_{\mathrm{pe}}$. Moreover, the velocities v_{ph} and v_{gr} do not vary in space, because the ionosphere is currently assumed homogeneous, i.e., $\omega_{\mathrm{pe}} = \mathrm{const}$. Thus, the only effect of the external magnetic field on signal propagation in formula (14) is the FR described by the factor $\mathbf{R}(\breve{\varphi}_{\mathrm{F}})$, where, unlike in (2), the angle $\breve{\varphi}_{\mathrm{F}}$ is no longer constant; see (15). The instantaneous frequency $\omega = \omega(t)$ in the expression (15) for $\breve{\varphi}_{\mathrm{F}}$ is given by (13). At the same time, we assume that the scattering formula (5) remains unchanged, which means, in particular, that the scattering is dispersionless, i.e., the matrix $\mathbf{S}$ does not depend on the frequency.

Introduce the two-way phase and group retarded times as

$$\mathfrak{t}_{\mathrm{ph,gr}}(t,z) \stackrel{\mathrm{def}}{=} t - 2R_z/v_{\mathrm{ph,gr}}(\omega_0), \tag{18}$$

and define (cf. formula (15))

$$\varphi_{\mathrm{F}}(t,z) = -\frac{R_z}{2c}\frac{\omega_{\mathrm{pe}}^2\Omega_{\mathrm{e}}}{\omega^2(\mathfrak{t}_{\mathrm{gr}}(t,z))} \equiv -\frac{R_z}{2c}\frac{\omega_{\mathrm{pe}}^2\Omega_{\mathrm{e}}}{\omega^2(t - 2R_z/v_{\mathrm{gr}}(\omega_0))}. \tag{19}$$

The dependence of φ_{F} on the signal time described by formula (19) will be called the differential Faraday rotation (dFR). Note that the definitions of $\mathfrak{t}_{\mathrm{ph,gr}}(t,z)$ correspond to the round-trip retardation (phase and group), while the FR angle $\varphi_{\mathrm{F}}(t,z)$ in (19) is only one half of the full round-trip FR angle. This notation will prove useful for future derivations. In particular, consider the scattering by a point target located at z and characterized by the matrix $\mathbf{S}$ (as defined by formula (5)). The signal received at the antenna is affected by the two-way transionospheric propagation subject to FR and the scattering event at the target, which occurs exactly at the middle of the round trip. Given that $\varphi_{\mathrm{F}}(t,z)$ of (19) equals one half of the round-trip FR angle, one can conveniently represent the received signal as follows (cf. formula (9)):

$$\mathbf{M}(t) = e^{-i\omega_0\mathfrak{t}_{\mathrm{ph}}(t,z)}A_{2\delta}(\mathfrak{t}_{\mathrm{gr}}(t,z))\mathbf{R}(\varphi_{\mathrm{F}}(t,z)) \cdot \mathbf{S} \cdot \mathbf{R}(\varphi_{\mathrm{F}}(t,z)), \tag{20}$$

where

$$A_{2\delta}(t) = \chi_{\tau-2\delta\tau}(t)e^{-i(\alpha+2\delta\alpha)t^2}. \tag{21}$$

In (21), $A_{2\delta}$ is the modified pulse envelope with twice the propagation effect on the chirp rate and duration compared to that in (16). Taking into account that whenever $A_{2\delta}(t) \neq 0$, $A_{2\delta}^{-1}(t) \equiv \overline{A_{2\delta}(t)}$ with the overbar denoting complex conjugate, one can easily invert (20) and obtain a counterpart of (10) for an LFM signal:

$$\mathbf{S} = e^{i\omega_0 \mathfrak{t}_{\mathrm{ph}}(t,z)}\overline{A_{2\delta}(\mathfrak{t}_{\mathrm{gr}}(t,z))}\mathbf{R}(-\varphi_{\mathrm{F}}(t,z)) \cdot \mathbf{M}(t) \cdot \mathbf{R}(-\varphi_{\mathrm{F}}(t,z)). \tag{22}$$

This relation can be verified directly for any t such that $|\mathfrak{t}_{\mathrm{gr}}(t,z)| \leqslant (\tau - 2\delta\tau)/2$ by substituting $\mathbf{M}(t)$ of (20) into the right-hand side of (22), using $\mathbf{R}(\varphi_1 + \varphi_2) = \mathbf{R}(\varphi_1) \cdot \mathbf{R}(\varphi_2)$, and arriving at the identity $\mathbf{S} = \mathbf{S}$. The latter means, in particular, that the right-hand side of (22) does not depend on t.

The scattering matrix $\mathbf{S}$ can be reconstructed from the data $\mathbf{M}(t)$ taken at any given moment of time t within the interval $|\mathfrak{t}_{\mathrm{gr}}(t,z)| \leqslant (\tau-2\delta\tau)/2$ where (22) is valid. One can also choose the expression that utilizes the entire interval; the result will be called the image and denoted by $\mathbf{I}$:

$$\mathbf{I} = \int e^{i\omega_0 \mathfrak{t}_{\mathrm{ph}}(t,z)}\overline{A_{2\delta}(\mathfrak{t}_{\mathrm{gr}}(t,z))}\mathbf{R}(-\varphi_{\mathrm{F}}(t,z)) \cdot \mathbf{M}(t) \cdot \mathbf{R}(-\varphi_{\mathrm{F}}(t,z))\, dt. \tag{23}$$

Note that there is no dependence of the image given by (23) on the coordinate; this will change in (25). The integration limits in (23) are determined by the indicator function in the definition of $A_{2\delta}(\mathfrak{t}_{\mathrm{gr}}(t,z))$; see (21). As the integrand in formula (23) is constant, the integral reduces to $\mathbf{I} = \tau''\mathbf{S}$, where $\tau'' = \tau - 2\delta\tau$ is the length of the integration interval (equal to the duration of the received chirp). The direct proportionality between the image $\mathbf{I}$ and the unknown quantity $\mathbf{S}$ is a key desired property of the polarimetric remote sensing system. Similarly to the exact reconstruction formula (10), it is achieved because the location z of the point scatterer is known ahead of time, and hence the integrand in (23) appears constant.

Let us now consider a more general imaging scenario, where instead of the point scatterer at a given fixed location we consider a distributed target. The reflectivity of the latter is described by the scattering matrix $\mathbf{S} = \mathbf{S}(z)$, which is defined according to the same indexing convention as in (5) and also becomes a function of the spatial coordinate z. Then, the received radar signal can be represented as follows (cf. formula (20)):

$$\mathbf{M}(t) = \int e^{-i\omega_0 \mathfrak{t}_{\mathrm{ph}}(t,z)} A_{2\delta}(\mathfrak{t}_{\mathrm{gr}}(t,z))\mathbf{R}(\varphi_{\mathrm{F}}(t,z)) \cdot \mathbf{S}(z) \cdot \mathbf{R}(\varphi_{\mathrm{F}}(t,z))\, dz. \tag{24}$$

In formula (24), we disregard the multiple scattering (see [10, Chapter 7] for more details).

Our goal is to reconstruct $\mathbf{S}(z)$ given $\mathbf{M}(t)$. The pointwise reconstruction formula (23) can be extended to the case of a distributed target as follows. First, we evaluate $\mathbf{S}$ according to (22) for every moment of time t, using the reference variable y instead of z, and then integrate the result over t as in (23). This yields the polarimetric image $\mathbf{I}(y)$:

$$\mathbf{I}(y) = \int e^{i\omega_0 \mathfrak{t}_{\mathrm{ph}}(t,y)}\overline{A_{2\delta}(\mathfrak{t}_{\mathrm{gr}}(t,y))}\mathbf{R}(-\varphi_{\mathrm{F}}(t,y)) \cdot \mathbf{M}(t) \cdot \mathbf{R}(-\varphi_{\mathrm{F}}(t,y))\, dt. \tag{25}$$

In the scalar case (where $\mathbf{R}$ is the identity matrix), formula (25) applies the matched filter

$$e^{i\omega_0 \mathsf{t}_{\rm ph}(t,y)}\overline{A_{2\delta}(\mathsf{t}_{\rm gr}(t,y))} \tag{26}$$

to the radar data. One can show that the matched filter (26) provides the best signal-to-noise ratio in the mean-square sense (i.e., in the sense of L_2) when the inversion of the data is done in the presence of noise; see, e.g., [4, section 4.1]. In the full vector case, formula (25) defines the polarimetric matched filter (PMF), which will be at the center of our study.

Note that in the mapping $\mathbf{M}(t) \mapsto \mathbf{I}(y)$ rendered by formula (25), the FR angle $\varphi_{\rm F}$ depends on the fast time t. To apply the PMF, one obviously needs to know this dependence explicitly. It is given by formula (19), and the corresponding parameters that characterize the ionosphere and the magnetic field of the Earth, namely, the plasma electron frequency $\omega_{\rm pe}$ and gyrofrequency $\Omega_{\rm e}$ (see (2)), are assumed available.

The integration limits in (25) are determined by $\operatorname{supp}\overline{A_{2\delta}(\mathsf{t}_{\rm gr}(t,y))}$. Substituting (24) and changing the order of integration, we obtain the imaging operator $\mathbf{S}(z) \mapsto \mathbf{I}(y)$:

$$\mathbf{I}(y) = \int dz\, e^{i\Phi} \int \overline{A_{2\delta}(\mathsf{t}_{\rm gr}(t,y))} A_{2\delta}(\mathsf{t}_{\rm gr}(t,z)) \mathbf{R}(\Delta\varphi_{\rm F}) \cdot \mathbf{S}(z) \cdot \mathbf{R}(\Delta\varphi_{\rm F})\, dt, \tag{27}$$

where

$$\Phi = -2k_0(y-z), \quad k_0 = k(\omega_0), \quad \Delta\varphi_{\rm F} \equiv \Delta\varphi_{\rm F}(t,y,z) = \varphi_{\rm F}(t,z) - \varphi_{\rm F}(t,y). \tag{28}$$

The kernel of the imaging operator (27), called the point spread function (PSF) and denoted by W, can be defined using tensor notation:

$$W_{iklj}(y,z) = e^{i\Phi} \int \overline{A_{2\delta}(\mathsf{t}_{\rm gr}(t,y))} A_{2\delta}(\mathsf{t}_{\rm gr}(t,z)) R_{ik}(\Delta\varphi_{\rm F}) R_{lj}(\Delta\varphi_{\rm F}) dt, \tag{29}$$

so that

$$I_{ij}(y) = \sum_{kl} \int W_{iklj}(y,z) S_{kl}(z)\, dz, \quad i,j,k,l \in \{\mathrm{H},\mathrm{V}\}. \tag{30}$$

In the case of single-polarization imaging, W is a scalar function of two spatial arguments, y and z (see, e.g., [10, Chapter 2]). Ideally, one would want to have $W \propto \delta(y-z)$, in which case the imaging operator provides the exact reconstruction. Due to the various limitations (e.g., a given fixed bandwidth), this cannot be achieved in practice, and real imaging systems are always subject to certain imperfections, such as finite resolution and the presence of sidelobes.

In the polarimetric case, W is a $2\times 2\times 2\times 2$ tensor whose entries are functions of the same two arguments y and z. The ideal coordinate dependence of each individual (nonzero) entry of this tensor would still be $W_{iklj} \propto \delta(y-z)$. Yet for a polarimetric system, there is another desired property. It has to do with the adequate representation of target reflectivities in different polarimetric channels relative to one another. We will call this property the polarimetric fidelity. In terms of the PSF, the higher the fidelity, the closer the desired tensor structure of the PSF to the one that keeps the scattering channels completely separate, i.e., $W_{iklj} \propto \delta_{ik}\delta_{lj}$. Indeed, all other nonzero entries of the tensor would contaminate the image in one channel by contributions due to other scattering channels. We will show that in the presence of FR, there will always be some level of contamination. Our goal is to obtain quantitative estimates of the contamination and propose an approach to its minimization.

3.2. PMF versus traditional polarimetry. At this point, it will be instrumental to compare the PMF procedure given by (25) with the traditional polarimetry in the presence of FR (see, e.g., [14, section 10.4]). The latter usually consists of two stages. At the first stage, the scalar matched filter (26) is applied to each channel separately, which yields the intermediate image matrix:

$$Y_{pq}(y) = \int e^{i\omega_0 \mathrm{t}_{\mathrm{ph}}(t,y)} \overline{A_{2\delta}(\mathrm{t}_{\mathrm{gr}}(t,y))} M_{pq}(t)\, dt, \quad pq \in \{\mathrm{HH}, \mathrm{HV}, \mathrm{VH}, \mathrm{VV}\}. \tag{31}$$

At the second stage, the rotation matrices $\mathbf{R}(-\varphi_{\mathrm{F}}^*)$ are applied to the intermediate image:

$$\mathbf{I}_{\mathrm{trad}}(y) = \mathbf{R}(-\varphi_{\mathrm{F}}^*) \cdot \mathbf{Y}(y) \cdot \mathbf{R}(-\varphi_{\mathrm{F}}^*). \tag{32}$$

The rotation angle φ_{F}^* used in formula (32) is constant, as if the signal were monochromatic. Substituting (24) and (31) into (32), one can show that the imaging operator in the case of traditional polarimetry is still given by (27), yet the expression (28) for $\Delta\varphi_{\mathrm{F}}$ changes:

$$\Delta\varphi_{\mathrm{F}} = \varphi_{\mathrm{F}}(t,z) - \varphi_{\mathrm{F}}^*. \tag{33}$$

The quantity φ_{F}^* in formula (33) can be thought of as an estimate of the FR angle for a certain distance $R^* = z^* - x$, taken at $\omega = \omega_0$:[6]

$$\varphi_{\mathrm{F}}^* = -\frac{\omega_{\mathrm{pe}}^2 \Omega_{\mathrm{e}}}{2c} \frac{R^*}{\omega_0^2}, \tag{34}$$

where z^* is a point in the target area. Because of the variation of the actual FR angle with frequency (i.e., dFR), the conventional polarimetric reconstruction (31), (32) involves a filter mismatch, which can be demonstrated by applying (27) to a point scatterer $\mathbf{S}(z) = \mathbf{S}_0\delta(z - z_0)$ and considering the resulting polarimetric image at $y = z_0$. Indeed, for the PMF case we will have a fully matched filter leading to $\mathbf{I}(z_0) = \tau''\mathbf{S}_0$ (as was the case for (23)), because the scalar part $\overline{A_{2\delta}(\,\cdot\,)}\, A_{2\delta}(\,\cdot\,)$ cancels out and the rotational part will consist of identity matrices due to (28): $\Delta\varphi_{\mathrm{F}}(t, z_0, z_0) \equiv 0$. However, the expression (33) for $\Delta\varphi_{\mathrm{F}}$ does not, generally speaking, turn into zero for all t even when $y = z_0 = z^*$. Hence, the rotational part of the imaging operator (27) cannot be fully compensated for. Therefore, some mismatch remains, and the proportionality relation between $\mathbf{I}(z_0)$ and $\mathbf{S}_0$ does not hold (one may, e.g., obtain a nonzero entry of the matrix $\mathbf{I}(z_0)$ that would correspond to a zero entry of the reflectivity matrix $\mathbf{S}_0$). In section 3.4, we will build the PSF for the traditional polarimetric processing and analyze the resulting distortions.

3.3. Performance estimate for the PMF. Let us introduce an alternative and, perhaps, more convenient representation of the imaging operator (27). It is obtained by recasting the 2×2 matrices $\mathbf{I}$ and $\mathbf{S}$ as four-dimensional vectors:

$$\boldsymbol{I}(y) = \int \mathbf{W}(y,z) \cdot \boldsymbol{S}(z)\, dz, \tag{35}$$

[6]Note that the intermediate image (31) offers a venue for estimating the FR angle φ_{F}^* from the received data; see, e.g., [6]. However, only the values of $\varphi_{\mathrm{F}}^* \mod \pi/4$ (or $\varphi_{\mathrm{F}}^* \mod \pi/2$ when some auxiliary data are available) can be reconstructed in this way. Although this approach does not take into account dFR, the resulting information appears sufficient for implementing the procedure described by (31), (32). Its outcome can be useful as long as dFR is small, as will be shown in section 3.4. However, the function $\varphi_{\mathrm{F}}(t, y)$ needed for the PMF approach (25) cannot, generally speaking, be reconstructed using this procedure. Indeed, for a P-band system with the parameters summarized in Table 1, the estimates of the FR angle yield $\varphi_{\mathrm{F}} \gg 1$.

where $\boldsymbol{I}(y) = (I_{\rm HH}, I_{\rm HV}, I_{\rm VH}, I_{\rm VV})^{\rm T}$ and $\boldsymbol{S}(y) = (S_{\rm HH}, S_{\rm HV}, S_{\rm VH}, S_{\rm VV})^{\rm T}$. In formula (35), $\mathbf{W}$ is a 4×4 matrix:

$$\mathbf{W}(y,z) = e^{i\Phi} \int \overline{A_{2\delta}(\mathfrak{t}_{\rm gr}(t,y))} A_{2\delta}(\mathfrak{t}_{\rm gr}(t,z)) \mathbf{V}(\Delta\varphi_{\rm F})\, dt, \tag{36}$$

where

$$\mathbf{V}(\phi) \stackrel{\rm def}{=} \begin{pmatrix} \cos^2\phi & -\cos\phi\sin\phi & \cos\phi\sin\phi & -\sin^2\phi \\ \cos\phi\sin\phi & \cos^2\phi & \sin^2\phi & \cos\phi\sin\phi \\ -\cos\phi\sin\phi & \sin^2\phi & \cos^2\phi & -\cos\phi\sin\phi \\ -\sin^2\phi & -\cos\phi\sin\phi & \cos\phi\sin\phi & \cos^2\phi \end{pmatrix}. \tag{37}$$

The ideal form of the matrices $\mathbf{V}(\Delta\varphi_{\rm F})$ and $\mathbf{W}(y,z)$ is diagonal, which is achieved if $\Delta\varphi_{\rm F} = 0$. However, in the presence of FR this condition does not hold unless $y = z$; see (28).

Recalling that the origin of the coordinate system is in the target area, we introduce

$$\varphi_{{\rm F}_0} = -\frac{|x|}{2c} \frac{\omega_{\rm pe}^2 \Omega_{\rm e}}{\omega_0^2} \tag{38}$$

as a scale of the total FR angle. We also assume that $|y| \ll |x|$ and $|z| \ll |x|$, which is typical for spaceborne SAR imaging. The calculation of $\Delta\varphi_{\rm F} = \varphi_{\rm F}(t,z) - \varphi_{\rm F}(t,y)$ requires some caution because the leading term $\varphi_{{\rm F}_0}$ cancels, while $|y-z|/|x| \ll 1$. For the expression

$$\Delta\varphi_{\rm F} = \varphi_{\rm F}(t,z) - \varphi_{\rm F}(t,y) \approx \frac{\partial\varphi_{\rm F}(t,z)}{\partial z} \cdot (z-y) \tag{39}$$

we have from (19)

$$\frac{\partial\varphi_{\rm F}(t,z)}{\partial z} = -\frac{\omega_{\rm pe}^2\Omega_{\rm e}}{2c} \frac{\partial}{\partial z} \frac{R_z}{\omega^2(\mathfrak{t}_{\rm gr}(t,z))} = -\frac{\omega_{\rm pe}^2\Omega_{\rm e}}{2c\omega^2} \Big(1 + 4\frac{R_z}{v_{\rm gr}(\omega_0)\tau}\frac{B}{\omega}\Big), \tag{40}$$

where we took into account that $\partial R_z/\partial z = 1$. The dependence of the right-hand side of (40) on t is via $\omega(\mathfrak{t}_{\rm gr}(t,z))$. However, as the variation of ω, i.e., the bandwidth, is small compared to the central carrier frequency, $B \ll \omega_0$, the leading term of (39) is obtained by replacing ω with ω_0 in (40). For similar reasons, we replace R_z with $|x|$ in (40) and get

$$\Delta\varphi_{\rm F} \approx \frac{\partial\varphi_{\rm F}(0,0)}{\partial z} \cdot (z-y) = -\frac{(z-y)}{2c} \frac{\omega_{\rm pe}^2\Omega_{\rm e}}{\omega_0^2} \Big(1 + 4\frac{|x|}{v_{\rm gr}(\omega_0)\tau}\frac{B}{\omega_0}\Big). \tag{41}$$

We will show below that if we use expression (41) for $\Delta\varphi_{\rm F}$, formula (36) reduces to

$$\mathbf{W}(y,z) = \mathbf{V}\big(\Delta\varphi_{\rm F}(\omega_0)\big) e^{i\Phi} \int \overline{A_{2\delta}(\mathfrak{t}_{\rm gr}(t,y))} A_{2\delta}(\mathfrak{t}_{\rm gr}(t,z))\, dt. \tag{42}$$

The integral on the right-hand side of (42) is encountered in the case of the scalar imaging as well. It can be evaluated by symmetrizing the integration interval (see [10, Chapters 2 and 3] for more details) and changing the integration variable $t \mapsto \tilde{t}$:

$$\tilde{t} = t - \frac{R_y + R_z}{v_{\rm gr}(\omega_0)} = t - \frac{y+z}{v_{\rm gr}(\omega_0)} - \frac{2|x|}{v_{\rm gr}(\omega_0)}, \quad T = \frac{R_y - R_z}{v_{\rm gr}(\omega_0)} = \frac{y-z}{v_{\rm gr}(\omega_0)}. \tag{43}$$

For simplicity, we will henceforth neglect the effect of ionospheric dispersion on the signal envelope given by (16) (see also (21)), i.e., drop the small corrections $|\delta\alpha|/\alpha = |\delta\tau|/\tau \lesssim 10^{-3}$ to the chirp rate and duration; see [8] and [10, section 3.2]. For the scalar case, when the corrections to the chirp parameters are incorporated into the filter as in (26), it has been shown in [10, section 3.11] that imaging with the corrected filter in the presence of dispersion[7] is essentially equivalent to the standard matched filter $e^{i\omega_0(t-2R_y/c)}\overline{A(t-2R_y/c)}$ for dispersionless propagation. While a similar analysis for the polarimetric case may require additional attention, hereafter we will rather concentrate on the dFR effects.

To show that (42) indeed holds, we will use $A(t)$ of (11) instead of $A_{2\delta}(t)$ defined in (21) and simplify the scalar part of the integrand in (36) (which is also the entire integrand in (42)) as follows:

$$\overline{A(\mathsf{t}_{\mathrm{gr}}(t,y))}A(\mathsf{t}_{\mathrm{gr}}(t,z)) = e^{-4i\alpha T\tilde{t}} \equiv e^{-2i\xi\tilde{t}/\tau}, \quad \text{where} \quad \xi = BT = B\frac{y-z}{v_{\mathrm{gr}}(\omega_0)}. \tag{44}$$

In (44), $|\tilde{t}| \leqslant \tau/2 - |T|$. Compared to (44), the dependence of $\mathbf{V}(\Delta\varphi_{\mathrm{F}})$ in (36) on $\tilde{t}$ (or, equivalently, t; see (43)) is slow. To show this, we take the time derivative of expression (28) and linearize the result with respect to $(y-z)$, as done in (39)–(41), to obtain

$$\frac{\partial\Delta\varphi_{\mathrm{F}}}{\partial\tilde{t}} \approx 2\frac{\xi}{\tau}\left[\varphi_{\mathrm{F}_0}\frac{v_{\mathrm{gr}}}{|x|\omega_0}\left(1+6\frac{|x|}{v_{\mathrm{gr}}(\omega_0)\tau}\frac{B}{\omega_0}\right)\right]. \tag{45}$$

The quantity in the square brackets on the right-hand side of (45) is much smaller than one. Hence, in the presence of the factor (44) under the integral in (36), we can disregard the dependence of $\mathbf{V}(\Delta\varphi_{\mathrm{F}})$ (see (37)) on the integration variable t. This justifies the use of expression (41) for $\Delta\varphi_{\mathrm{F}}$, so that (36) is reduced to (42).

We have $\operatorname{supp}\overline{A(\mathsf{t}_{\mathrm{gr}}(t,y))}\bigcap\operatorname{supp}A(\mathsf{t}_{\mathrm{gr}}(t,z)) \neq \emptyset$ as long as $\tau - 2|T| \geqslant 0$, or $|\xi| \leqslant B\tau/2$. Performing the integration in (42), we introduce (see [10, section 2.4] for more details)

(46)
$$F^{(B\tau)}(\xi) = \chi_{B\tau}(\xi)\frac{1}{\tau}\int_{-\tau/2+|T|}^{\tau/2-|T|} e^{-2i\xi\tilde{t}/\tau}d\tilde{t} = \chi_{B\tau}(\xi)\left(1-\frac{2|\xi|}{B\tau}\right)\operatorname{sinc}\left[\xi\left(1-\frac{2|\xi|}{B\tau}\right)\right],$$

where $\operatorname{sinc}\xi \stackrel{\text{def}}{=} \sin\xi/\xi$ and the indicator function χ is defined in (12). Then,

$$\mathbf{W}(y,z) = \mathbf{V}(\Delta\varphi_{\mathrm{F}})e^{i\Phi}\tau F^{(B\tau)}(\xi) \equiv \mathbf{V}(\Delta\varphi_{\mathrm{F}})W^{(B\tau)}(\xi), \tag{47}$$

where we have defined the scalar PSF as

$$W^{(B\tau)}(\xi) \stackrel{\text{def}}{=} \tau e^{i\Phi}F^{(B\tau)}(\xi). \tag{48}$$

The function $W^{(B\tau)}(\xi)$ given by (48), which is a common factor in the expressions for all polarimetric channels, can indeed be interpreted as the PSF for single-channel imaging. It would relate a scalar image $I(y)$ to a scalar reflectivity function $S(z)$ via a scalar counterpart of (35) (or (30)). Typically, for high-resolution imaging the compression ratio of the chirp is high: $B\tau \gg 1$. Then, for $|\xi| \ll B\tau$ we can

[7] This filter is the same as the one that appears in the scalar part of the integrand on the right-hand side of (25).

replace $\big(1-2|\xi|/(B\tau)\big)$ in (46) with one. Accordingly, the functions $F^{(B\tau)}(\xi)$ of (46) and $W^{(B\tau)}(\xi)$ of (48) simplify to

$$\mathcal{F}(\xi) \stackrel{\text{def}}{=} \frac{1}{\tau}\int_{-\tau/2}^{\tau/2} e^{-2i\xi\tilde{t}/\tau}d\tilde{t} = \int_{-1/2}^{1/2} e^{-2i\xi u}du = \operatorname{sinc}\xi \tag{49}$$

and

$$\mathcal{W}(\xi) \stackrel{\text{def}}{=} \tau e^{i\Phi}\mathcal{F}(\xi) \equiv \tau e^{i\Phi}\operatorname{sinc}\xi, \tag{50}$$

respectively. The main lobe of the scalar PSF $\mathcal{W}(\xi)$ given by (50) corresponds to the following interval of its argument: $|\xi| \leqslant \pi$. Equivalently, we have

$$|R_y - R_z| \equiv |y-z| \leqslant \Delta_{\mathrm{R}} \equiv \frac{\pi c}{B}, \tag{51}$$

where Δ_{R} is called the resolution.[8] The use of $\mathcal{W}$ instead of $W^{(B\tau)}$ is justified for the main lobe of the PSF because $|\xi| \leqslant \pi$ implies $|\xi| \ll B\tau$ (see [10, section 2.4] for details).

Let us now introduce

$$\eta = -\varphi_{\mathrm{F}_0}\frac{2B}{\omega_0}, \tag{52}$$

where φ_{F_0} is given by (38). In section 3.4, it will be shown (see, in particular, formula (70)) that it is the parameter η of (52) that controls the magnitude of the dFR effect in the case of traditional polarimetric SAR processing. In the meantime, analyzing the last factor on the right-hand side of (41) and taking the typical values from Table 1, we notice that $4|x|B/\big(v_{\mathrm{gr}}(\omega_0)\tau\omega_0\big) \gtrsim 1$. For future convenience, let us also recast $\Delta\varphi_{\mathrm{F}}$ of (41) as

$$\Delta\varphi_{\mathrm{F}} = \frac{2C_\tau}{B\tau}\eta\xi, \quad \text{where} \quad C_\tau = 1 + \frac{\omega_0}{4B}\frac{v_{\mathrm{gr}}(\omega_0)\tau}{|x|} = \mathcal{O}(1). \tag{53}$$

The 4×4 matrix $\mathbf{W}$ given by (36), (37) has only three different entries (up to the sign):

$$\mathbf{W} = \begin{pmatrix} W_0 & -W_1 & W_1 & -W_2 \\ W_1 & W_0 & W_2 & W_1 \\ -W_1 & W_2 & W_0 & -W_1 \\ -W_2 & -W_1 & W_1 & W_0 \end{pmatrix}, \tag{54}$$

where

$$W_0(\xi,\eta) = \cos^2\left(\frac{2C_\tau}{B\tau}\eta\xi\right)W^{(B\tau)}(\xi), \tag{55a}$$

$$W_1(\xi,\eta) = \cos\left(\frac{2C_\tau}{B\tau}\eta\xi\right)\sin\left(\frac{2C_\tau}{B\tau}\eta\xi\right)W^{(B\tau)}(\xi), \tag{55b}$$

$$W_2(\xi,\eta) = \sin^2\left(\frac{2C_\tau}{B\tau}\eta\xi\right)W^{(B\tau)}(\xi), \tag{55c}$$

[8] In the context of SAR, the quantity Δ_{R} is specifically referred to as the range resolution. Note that the expression on the right-hand side of (51) contains the speed of light c rather than the group velocity $v_{\mathrm{gr}}(\omega_0)$ that helps define ξ in (44). This simplification is possible because for the typical parameters of interest given in Table 1 the difference between the two velocities is small (see [10, section 3.8] for further details).

and ξ is proportional to $(y-z)$; see (44). The explicit dependence of the PSF on η that we have introduced in (55) will later facilitate the comparison of the PMF with traditional polarimetric SAR processing. For the typical parameters given in Table 1, we have $|\eta| \lesssim 1$. Therefore, within the main lobe of the PSF $\mathcal{W}(\xi)$ of (50), $|\xi| \leqslant \pi$, the argument of the trigonometric functions in (55) is small, so the following relations hold:

$$W_0 \approx \mathcal{W} \quad \text{and} \quad |W_p| = \mathcal{O}\big(\tau \cdot (B\tau)^{-p}\big), \quad p = 0, 1, 2.$$

In particular, we see that the image of a point scatterer in the vicinity of its maximum is insignificantly affected by FR (because $B\tau \gg 1$).

To provide a quantitative assessment of polarimetric contamination, let us first recall some key measures of radar performance in the single-polarization case. To do so, we write down the scalar counterpart of (35):

$$I(y) = \int W(y,z) S(z) dz, \tag{56}$$

where $W(y,z) = \mathcal{W}(\xi)$ is given by (50). As has been mentioned previously (see the discussion at the end of section 3.1), we would ideally want the PSF in (56) to be equal to the δ-function, $W(y,z) = \delta(y-z)$, in which case the image $I(y)$ would coincide with the target reflectivity $S(z)$. In reality, this cannot be expected, and it is therefore important to be able to quantify the difference between the actual PSF and the corresponding δ-function. One of the commonly used metrics is the width of the main lobe of $\mathcal{W}(\xi)$, i.e., the resolution size Δ_{R}; see (51). To characterize the role of the sidelobes, i.e., those y for which $|y-z| > \Delta_{\mathrm{R}}$, one can employ the integrated sidelobe ratio (ISLR). ISLR is defined as the ratio of the power in the sidelobes of a PSF to that in its main lobe, and is usually measured in decibels (see, e.g., [5, section 2.8]). For the simplified PSF $\mathcal{W}(\xi)$ defined in (50), the main lobe is given by $|\xi| \leqslant \pi$, and it can be shown that

$$\mathrm{ISLR}(\mathcal{W}) = 10 \log_{10} \left[\left(\int_{|\xi|>\pi} |\mathcal{W}(\xi)|^2 \, d\xi \right) \left(\int_{|\xi|\leqslant\pi} |\mathcal{W}(\xi)|^2 \, d\xi \right)^{-1} \right]. \tag{57}$$

Given that $\mathcal{W}(\xi) \propto \operatorname{sinc} \xi$ in (50), the right-hand side of formula (57) evaluates to approximately $-9.68dB$. This means that about 90% of the total power of $\mathcal{W}$ is contained in its main lobe. In other words, the ISLR basically shows how well defined the central peak is compared to the background given by sidelobes. As sidelobes can be thought of as "spreading," one can also say that ISLR indicates to what extent a given point source may adversely affect other areas of the image. The ISLR is of key importance for the analysis of distributed radar targets.

To define the ISLR for a more general PSF $W^{(B\tau)}(\xi)$ of (48), we first notice that its main lobe is given by $|\xi(1-\frac{2|\xi|}{B\tau})| \leqslant \pi$; see (46). For $B\tau \gg 1$, this is approximately equivalent to $|\xi| \leqslant \pi + \frac{2\pi^2}{B\tau}$, and the integration intervals in the definition of ISLR should, technically speaking, be changed accordingly. However, while this new interval of ξ is not the same as $|\xi| \leqslant \pi$, it is very close to $|\xi| \leqslant \pi$ because $\frac{2\pi^2}{B\tau} \ll \pi$ (see [10, section 2.4] for more details). As the value of $|W^{(B\tau)}(\xi)|^2$ in the vicinity of $\xi = \pi$ is also small, one can expect that the effect of changing the integration interval on the resulting value of ISLR will be negligible. As such, hereafter we will take $|\xi| \leqslant \pi$ as the definition of the main lobe of $W^{(B\tau)}$. This yields[9]

$$\text{ISLR}(W^{(B\tau)}) \stackrel{\text{def}}{=} 10\log_{10}\left[\left(\int_{|\xi|>\pi} |W^{(B\tau)}(\xi)|^2\, d\xi\right)\left(\int_{|\xi|\leqslant\pi} |W^{(B\tau)}(\xi)|^2\, d\xi\right)^{-1}\right]. \tag{58}$$

As for the matrix PSF $\mathbf{W}$ given by (54), its diagonal entry W_0 differs from $W^{(B\tau)}(\xi)$ of (48) by the factor $\cos^2(\,\cdot\,)$; see (55a). This factor is equal to 1 if $\eta = 0$, but one can show that for η varying within $|\eta| \leqslant 2.5$, the corresponding value of ISLR(W_0) defined as in (58) will exhibit only insignificant variations—by no more than $0.1dB$. Hence, about 90% of the total power of W_0 is contained in its main lobe as well. It should be noted, though, that in real systems the sidelobes (and, hence, the ISLR) are affected by several additional factors such as the antenna radiation pattern. On the other hand, the ISLR can be lowered, e.g., by introducing amplitude windowing in the filter (26); see, e.g., [5, section 2.6]. The effect of windowing will not be considered in the current paper.

In the case of polarimetric imaging, the cross-channel contamination presents an additional source of image distortions, beyond the finite (nonzero) resolution and the spreading characterized by ISLR. This contamination manifests itself through the off-diagonal entries of the matrix $\mathbf{W}$ of (54). Indeed, if $\mathbf{W}$ were diagonal, then the image in each of the four polarization channels would have been characterized by the scalar PSF W_0 of (55a) completely independently of the three remaining channels. Yet in reality a more complex scenario transpires where the radar performance in a given channel is affected by contributions from all other channels.

To quantify the cross-channel contamination, we need to compare the magnitude of the off-diagonal entries of $\mathbf{W}$ relative to that of its diagonal entries. To do so, let us first introduce $\mathbf{D} \stackrel{\text{def}}{=} \operatorname{diag}\mathbf{W} = \operatorname{diag}\{W_0, W_0, W_0, W_0\}$. Then, the relative magnitude of the off-diagonal entries can be characterized by the quantity

$$\|\mathbf{W} - \mathbf{D}\| \cdot \|\mathbf{D}\|^{-1}, \tag{59}$$

where $\|\ \ldots\ \|$ is an appropriate norm on the space of 4×4 matrices. As all norms on linear spaces of finite dimension are equivalent, we can choose one that would be easy to evaluate. Hereafter, we will be using the Frobenius norm, which is the l_2 norm of a 4×4 matrix interpreted as a vector with 16 components; see, e.g., [12, Chapter 5].

However, when evaluating the norms in (59), one also needs to take into account that the entries of $\mathbf{W}$ (and $\mathbf{D}$) are functions rather than plain numbers; see formulae (55). Therefore, the quantity (59) itself becomes a function of the argument ξ, whereas η remains a parameter that characterizes the dFR effect; see (52). Accordingly, to provide a comprehensive measure of the cross-channel contamination, we integrate with respect to ξ and replace (59) with

$$\begin{aligned}\left(\int \|\mathbf{W} - \mathbf{D}\|^2 d\xi\right)&\left(\int \|\mathbf{D}\|^2 d\xi\right)^{-1} \\ &= \left(\int \left(2|W_1(\xi,\eta)|^2 + |W_2(\xi,\eta)|^2\right) d\xi\right)\left(\int |W_0(\xi,\eta)|^2 d\xi\right)^{-1}.\end{aligned} \tag{60}$$

[9]For $B\tau = 2\pi\cdot 400$ as in Table 1, the right-hand side of (58) evaluates to roughly $-9.7dB$. The difference between this value and that in (57) is due to a finite support of $W^{(B\tau)}$, while the effect of changing the integration limits in (58) from $|\xi| = \pi$ to the actual boundaries of the main lobe of $W^{(B\tau)}$ would be even smaller.

For future convenience, we are using the square of the Frobenius norm in formula (60) rather than the plain norm as in (59). The right-hand side of (60) was obtained by taking into account the actual structure of the matrix $\mathbf{W}$ of (54). The quantity (60) appears at least superficially similar to the one under the logarithm in the definition of ISLR; see (57) and (58).

The integration limits are not yet specified explicitly in formula (60). This can be done in a variety of ways, which allows us to introduce (at least) two somewhat different measures of the cross-channel contamination; see sections 3.3.1 and 3.3.2.

3.3.1. Point-based polarimetric contamination metric. First, we construct a metric that applies to point targets. In this case, one may be interested in quantifying the distortions in a given polarimetric channel due to the contributions from the other channels at the same point, as opposed to the sidelobes of the same channel that characterize the spreading. Then, the integration in (60) shall be performed over the main lobe of the diagonal entries of the PSF, because it is this lobe that yields the "useful" part of the image of a point target. For the diagonal PSF $W_0(\xi)$, the main lobe is taken as $|\xi| \leqslant \pi$ per the discussion that precedes formula (58). This leads to the following definition of what we will call the point-based polarimetric contamination metric (PPCM):

$$\text{PPCM}(\mathbf{W},\eta) \stackrel{\text{def}}{=} 10\log_{10}\left[\left(\int_{|\xi|\leqslant\pi}\left(2|W_1(\xi,\eta)|^2+|W_2(\xi,\eta)|^2\right)d\xi\right)\cdot\left(\int_{|\xi|\leqslant\pi}|W_0(\xi,\eta)|^2 d\xi\right)^{-1}\right]. \tag{61}$$

Note that on the left-hand side of formula (61) we have specified the explicit dependence on η, while on the right-hand side we use the logarithm of the quantity introduced in (60) to make the result look similar to the ISLR of (57) or (58).

Due to the factor $\sin(\Delta\varphi_{\text{F}}) = \sin\left(\frac{2C_\tau}{B\tau}\eta\xi\right)$ present in both W_1 and W_2 (see formulae (55b) and (55c)), the first integral on the right-hand side of (61) appears very small. Indeed, using $|\sin\xi| \leqslant |\xi|$ and $|\cos\xi| \leqslant 1$, we obtain

$$\int_{|\xi|\leqslant\pi}|W_1(\xi,\eta)|^2\,d\xi \lesssim 2\pi\tau^2\Big(\frac{2C_\tau}{B\tau}\eta\Big)^2,\quad \int_{|\xi|\leqslant\pi}|W_2(\xi,\eta)|^2\,d\xi \lesssim \frac{2\pi^3}{3}\tau^2\Big(\frac{2C_\tau}{B\tau}\eta\Big)^4. \tag{62}$$

At the same time, according to the definition of ISLR, the second integral in (61) is about $0.9\cdot\pi\tau^2$ (see (57)). Then, given that for the parameters from Table 1 we have

$$10\log_{10}\frac{1}{B\tau} \approx -34dB, \tag{63}$$

the PPCM$(\mathbf{W},\eta)$ of (61) will not exceed $-60dB$ for $|\eta| \lesssim 1$. From the discussion in section 5, we will see that in practice such a low level of distortions can be completely disregarded.

3.3.2. Area-based polarimetric contamination metric. An alternative metric can be built that would apply to distributed rather than point targets. For a distributed target, the image intensity at a certain point includes contributions from the sidelobes of scatterers located around this point. To account for the sidelobes, we integrate over the entire real axis in (60) and introduce the area-based polarimetric contamination metric (APCM) (cf. formula (61)),

$$\text{APCM}(\mathbf{W},\eta) \stackrel{\text{def}}{=} 10\log_{10}\frac{2\|W_1\|_2^2(\eta)+\|W_2\|_2^2(\eta)}{\|W_0\|_2^2(\eta)}, \tag{64}$$

where for a function of two variables $f = f(\xi,\eta)$, its L_2 norm is obtained by integration with respect to ξ, while η remains a parameter:

$$\|f\|_2^2(\eta) \stackrel{\text{def}}{=} \int_{-\infty}^{\infty} |f(\xi,\eta)|^2 d\xi. \tag{65}$$

In evaluating the APCM, we expect that $\|W_1\|_2$ and $\|W_2\|_2$ will be small. The reason for this, similarly to the case of PPCM (61), is the factor $\sin(\Delta\varphi_{\text{F}}) = \sin\left(\frac{2C_\tau}{B\tau}\eta\xi\right)$ present in W_1 and W_2; see (55b) and (55c). As a function of $|\xi|$, this factor peaks well outside $\operatorname{supp} W^{(B\tau)}(\xi) \equiv \operatorname{supp}\chi_{B\tau}(\xi)$, while near the maximum of $|W^{(B\tau)}(\xi)|$, this factor is small. Recalling once again that $|\sin\xi| \leqslant |\xi|$, $|\cos\xi| \leqslant 1$, we obtain the following estimates: $|W_1(\xi,\eta)| \leqslant \tau\left|\frac{2C_\tau}{B\tau}\eta\right|$ and $|W_2(\xi,\eta)| \leqslant \tau\left|\frac{2C_\tau}{B\tau}\eta\right|^2|\xi|$. Then, taking into account that $\operatorname{supp} F^{(B\tau)}(\xi) \subset (-B\tau/2, B\tau/2)$ and $|F^{(B\tau)}(\xi)| \leqslant 1$, we have

$$\|W_1\|_2^2 \leqslant \tau^2\frac{4}{B\tau}C_\tau^2\eta^2, \quad \|W_2\|_2^2 \leqslant \tau^2\frac{4}{3B\tau}C_\tau^4\eta^4. \tag{66}$$

At the same time, for $\|W_0\|_2$ the bulk of the integral (65) comes from the main lobe $|\xi| \leqslant \pi$, per the discussion that follows (57). Then, replacing $\cos^2(\cdot)$ and $W^{(B\tau)}$ in the definition of W_0 in (55) with 1 and $\mathcal{W}$, respectively, we obtain $\|W_0\|_2^2 \approx \|\mathcal{W}\|_2^2 = \pi\tau^2$. Using (66) in (64), we arrive at the following estimate for the APCM:

$$\text{APCM}(\mathbf{W},\eta) \lesssim 10\log_{10}\left(\frac{1}{B\tau}\frac{4}{\pi}\Big(2C_\tau^2\eta^2 + \frac{1}{3}C_\tau^4\eta^4\Big)\right). \tag{67}$$

Though much greater than the estimates for PPCM,[10] the values of APCM given by (67) are still below $-30dB$ even for $|\eta| \sim 1$ (see (63) and (53)), whereas for $|\eta| \ll 1$ they are considerably smaller. We can thus conclude that the resulting polarimetric contamination is negligible for most practical purposes (see section 5 for a brief discussion of the relevant SAR applications). This is achieved because of a low level of the residual mismatch guaranteed by the application of the PMF (see formulae (41) and (45)).

In the next section, we show that in the case of the traditional polarimetric SAR processing, as opposed to the PMF, the distortions of images due to dFR may be much larger.

3.4. Performance estimate for the traditional SAR polarimetry. As indicated in section 3.2, the traditional polarimetric processing (see, e.g., [14, section 10.4]) takes a certain value of the FR angle φ_{F}^* (see (34)) that is assumed constant across the entire image (unlike in (25)), as if the radar pulse were monochromatic. The imaging operator $\mathbf{S}(z) \mapsto \mathbf{I}(y)$ for the traditional polarimetric SAR is described by the same expression (27) as the PMF operator, while expression (28) for $\Delta\varphi_{\text{F}}$ is replaced with (33): $\Delta\varphi_{\text{F}} = \varphi_{\text{F}}(t,z) - \varphi_{\text{F}}^*$. The quantity $\varphi_{\text{F}}^* = \varphi_{\text{F}}(t^*,z^*)$ can also be represented

[10]This can be seen by comparing the powers of $B\tau$ in the argument of $\log_{10}$ in (67) with those on the right-hand sides of (62).

by formula (19), where z^* is the same as in (34) and t^* is such that $\mathfrak{t}_{\rm gr}(t^*,z^*)=0$, i.e., $t^*=2R^*/v_{\rm gr}(\omega_0)$. Then,

$$\Delta\varphi_{\rm F}=\Delta\varphi_{\rm F}(t,z)=-\frac{\omega_{\rm pe}^2\Omega_{\rm e}}{2c}\left(\frac{R_z}{\omega^2(\mathfrak{t}_{\rm gr}(t,z))}-\frac{R^*}{\omega_0^2}\right). \tag{68}$$

As the FR angle varies with frequency (which is the effect of dFR), expression (68) shows that there is a filter mismatch for all y (coordinate of the image) and z (coordinate of the target). We are going to estimate the resulting image distortions.

We approximate $\Delta\varphi_{\rm F}(t,z)$ by expanding $\varphi_{\rm F}(t,z)$ in Taylor series near z^* and t^*:

$$\varphi_{\rm F}(t,z)\approx-\frac{\omega_{\rm pe}^2\Omega_{\rm e}}{2c}\left[\frac{R^*}{\omega_0^2}+\frac{\partial}{\partial z}\frac{R_z}{\omega^2(\mathfrak{t}_{\rm gr}(t,z))}\bigg|_{t^*,z^*}(z-z^*)+R^*\,\frac{\partial}{\partial t}\frac{1}{\omega^2(\mathfrak{t}_{\rm gr}(t,z))}\bigg|_{t^*,z^*}(t-t^*)\right].$$

Then, with the help of (34), (38), and (43), formula (68) yields

$$\Delta\varphi_{\rm F}=\varphi_{{\rm F}_0}\left[\frac{(z-z^*)}{|x|}-\frac{2B}{\omega_0}\frac{R^*}{|x|}\frac{T}{\tau}-\frac{2B}{\omega_0}\frac{R^*}{|x|}\frac{\tilde t}{\tau}\right]. \tag{69}$$

The first term in the brackets on the right-hand side of (69) represents the variation of the FR angle at the carrier frequency over the image. The absolute value of this term is controlled by the size of the image and the accuracy of reconstruction of $\varphi_{\rm F}^*$. For large images, the standard polarimetric procedure can easily be adjusted for this effect, e.g., by segmenting the image. As this term is not related to dFR, we will not consider it hereafter.

To estimate the second term, we notice that in our development of the SAR ambiguity theory, we are primarily interested in considering the locations y and z that would be sufficiently close to one another, within the resolution distance as defined by (51). Then, for the quantity T introduced in (43), we can assume that $|T|\lesssim 1/B$. Given also that $R^*\approx|x|$, the absolute value of the second term on the right-hand side of (69) appears to be about $\frac{2}{\omega_0\tau}$. The third term depends on $\tilde t$ and reaches B/ω_0 at the endpoints of the interval $(-\frac{\tau}{2},\frac{\tau}{2})$. The latter value is about $B\tau\gg 1$ times larger than the estimate of the second term.[11] Hence, only the largest term on the right-hand side of (69) will be included into our subsequent analysis:

$$\Delta\varphi_{\rm F}\approx-\varphi_{{\rm F}_0}\frac{2B}{\omega_0}\frac{\tilde t}{\tau}=\eta\frac{\tilde t}{\tau}, \tag{70}$$

where the parameter η is still defined by (52). Taking into account that $\varphi_{\rm F}^*=\text{const}$ in (33), we can see from (70) that the variation of the FR angle over the duration of the pulse is equal to the absolute value of η because $|\tilde t/\tau|\leqslant 1/2$.

To distinguish between the PMF and traditional processing, we will denote the traditional PSF matrix by $\tilde{\mathbf{W}}$. The structure of $\tilde{\mathbf{W}}$ is similar to that of $\mathbf{W}$; see (54). The three different entries (up to the sign) $\tilde W_0$, $\tilde W_1$, and $\tilde W_2$ can be obtained using the double angle formulae in (36), (37) (e.g., $\cos^2\Delta\varphi_{\rm F}=(1+\cos(2\Delta\varphi_{\rm F}))/2$) and also

[11] It is easy to see that the second term is similar to that in the PMF case (see (53)), accurate to a factor $C_\tau=\mathcal{O}(1)$.

with the help of (44):

$$
\begin{aligned}
\tilde{W}_0(\xi,\eta) &\stackrel{\text{def}}{=} e^{i\Phi}\int_{-\tau/2}^{\tau/2} e^{-2i\xi\tilde{t}/\tau}\cos^2(\Delta\varphi_{\text{F}})d\tilde{t} = \frac{\tau e^{i\Phi}}{2}\big(\mathcal{F}(\xi)+F_0(\xi,\eta)\big),\\
\tilde{W}_1(\xi,\eta) &\stackrel{\text{def}}{=} e^{i\Phi}\int_{-\tau/2}^{\tau/2} e^{-2i\xi\tilde{t}/\tau}\cos(\Delta\varphi_{\text{F}})\sin(\Delta\varphi_{\text{F}})d\tilde{t} = \frac{\tau e^{i\Phi}}{2i}F_1(\xi,\eta),\\
\tilde{W}_2(\xi,\eta) &\stackrel{\text{def}}{=} e^{i\Phi}\int_{-\tau/2}^{\tau/2} e^{-2i\xi\tilde{t}/\tau}\sin^2(\Delta\varphi_{\text{F}})d\tilde{t} = \frac{\tau e^{i\Phi}}{2}\big(\mathcal{F}(\xi)-F_0(\xi,\eta)\big),
\end{aligned}
\tag{71}
$$

where $\mathcal{F}(\xi)=\operatorname{sinc}\xi$ is defined in (49) and we have additionally introduced the notation

$$
\begin{aligned}
F_0(\xi,\eta) &= \frac{1}{\tau}\int_{-\tau/2}^{\tau/2} e^{-2i\xi\tilde{t}/\tau}\cos(2\eta\tilde{t}/\tau)\,d\tilde{t} = \frac{1}{2}\big(\operatorname{sinc}(\xi-\eta)+\operatorname{sinc}(\xi+\eta)\big),\\
F_1(\xi,\eta) &= \frac{i}{\tau}\int_{-\tau/2}^{\tau/2} e^{-2i\xi\tilde{t}/\tau}\sin(2\eta\tilde{t}/\tau)\,d\tilde{t} = \frac{1}{2}\big(\operatorname{sinc}(\xi-\eta)-\operatorname{sinc}(\xi+\eta)\big).
\end{aligned}
\tag{72}
$$

Dependence of the integration limits on $T=\xi/B$ has been dropped in (71) and (72) (cf. formula (46)). One can show that this dependence has a negligibly small effect on the results of calculations in this section.

While $\max_\xi|\mathcal{F}(\xi)|=1$, we have $\max_{\xi,\eta}|F_0(\xi,\eta)|=1$ and

$$
\max_{\xi,\eta}|F_1(\xi,\eta)|\approx 0.6=\mathcal{O}(1)\quad\text{attained at}\quad |\xi|=|\eta|=\frac{1}{2}|\arg\min_{\zeta}\operatorname{sinc}\zeta|\approx 2.2.
\tag{73}
$$

If $\eta=0$, we have $F_0(\xi,0)\equiv\mathcal{F}(\xi)$ and $F_1(\xi,0)\equiv 0$, so $\tilde{W}_0(\xi,0)\equiv\mathcal{W}(\xi)$ (see (50)) and $\tilde{W}_1(\xi,0)\equiv\tilde{W}_2(\xi,0)\equiv 0$. In other words, for $\eta=0$ the polarimetric contamination vanishes and the matrix $\tilde{\mathbf{W}}$ becomes diagonal.

For an arbitrary η, a direct calculation using (71) in (64) yields

$$
\operatorname{APCM}(\tilde{\mathbf{W}},\eta) = 10\log_{10}\frac{5-\operatorname{sinc}2\eta-4\operatorname{sinc}\eta}{3+4\operatorname{sinc}\eta+\operatorname{sinc}2\eta}.
\tag{74}
$$

While no analytic expressions for $\operatorname{PPCM}(\tilde{\mathbf{W}})$ are available, the corresponding quadratures can easily be computed numerically. We present the plots of $\operatorname{PPCM}(\tilde{\mathbf{W}},\eta)$ and $\operatorname{APCM}(\tilde{\mathbf{W}},\eta)$ in Figure 1.[12]

If $|\eta|\ll 1$, then we can also obtain the following asymptotic expressions for the entries of the matrix $\tilde{\mathbf{W}}$:

$$
\begin{aligned}
\tilde{W}_0(\xi,\eta) &\approx \tau e^{i\Phi}\left[\operatorname{sinc}\xi-\eta^2\frac{2\xi\cos\xi+(\xi^2-2)\sin\xi}{4\xi^3}\right],\\
\tilde{W}_1(\xi,\eta) &\approx \frac{1}{i}\tau e^{i\Phi}\eta\frac{\sin\xi-\xi\cos\xi}{2\xi^2},\\
\tilde{W}_2(\xi,\eta) &\approx \tau e^{i\Phi}\eta^2\frac{2\xi\cos\xi+(\xi^2-2)\sin\xi}{4\xi^3}.
\end{aligned}
\tag{75}
$$

[12]Fixed integration limits given in formula (61) are still used for the calculation of $\operatorname{PPCM}(\tilde{\mathbf{W}})$, even though the width of the main lobe of $\tilde{W}_0$, which is the diagonal entry of $\tilde{\mathbf{W}}$, depends on η; see (71). The rationale is that the fraction of energy in the main lobe of $\tilde{W}_0$ that is outside the fixed interval $(-\pi,\pi)$ can be shown to be no greater than 10^{-4} for the entire plotted range of η.

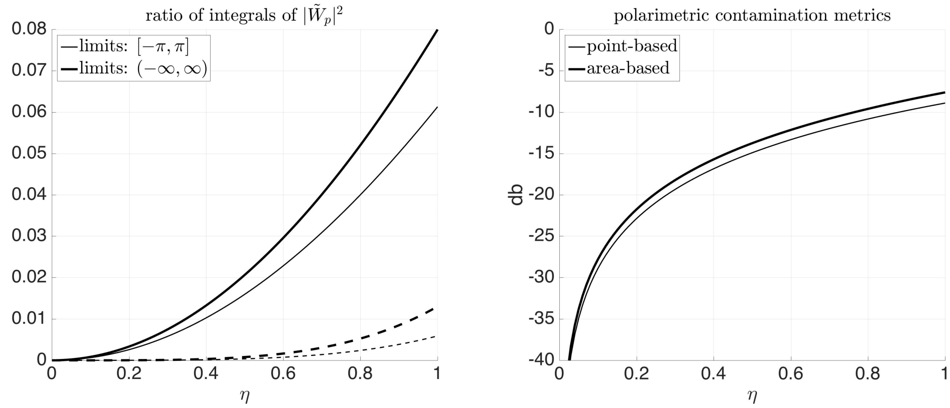

FIG. 1. *Left panel: Plots of* $\left(\int |\tilde{W}_p(\xi,\eta)|^2 d\xi\right)\left(\int |\tilde{W}_0(\xi,\eta)|^2 d\xi\right)^{-1}$ *for* $p = 1$ *(solid line) and* $p = 2$ *(dashed line) (cf. formula* (60)*). Right panel: Comparison of the two metrics of polarimetric error for traditional polarimetry.*

All three fractions in (75) are regular functions of ξ in the vicinity of $\xi = 0$, and are at most $\mathcal{O}(1)$. As $|\eta| \to 0$, we can derive from (74) (cf. formula (67))

$$\text{APCM}(\tilde{\mathbf{W}},\eta) \approx 10\log_{10}\frac{\eta^2}{6}. \tag{76}$$

Obviously, the leading term in the expression for APCM given by (76) is due to $\tilde{W}_1$ in (74); see formulae (75) and Figure 1. Expression (76) yields the errors that are much larger than those for the PMF case because there is a large factor of $B\tau \gg 1$ in the denominator of (67).

We should also note that the distortion metrics we have introduced may still fail to provide a complete characterization of the resulting image matrix $\tilde{\mathbf{I}}(y)$ and its "deviation" from the original scatterer $\mathbf{S}(z)$. Notice, for example, that $\tilde{W}_0$ is an even function of ξ with a peak at $\xi = 0$, whereas $\tilde{W}_1$ is an odd function of ξ; see (71), (72). Consider a hypothetical point target, $\mathbf{S}(z) = \mathbf{S}_0\delta(z - z_0)$, with S_{HH} as the only nonzero entry of the scattering matrix $\mathbf{S}_0$. The corresponding image in the HH-channel, i.e., $\tilde{I}_{\text{HH}}(y)$, will have a single peak, whereas $\tilde{I}_{\text{HV}}(y)$ will have two intensity peaks separated by a distance comparable to the resolution size; see (75) and (73). More sophisticated distortion criteria may be needed to capture this or similar effects.

3.5. Summary for the single-pulse case. Our main observation thus far has been that the polarimetric fidelity of the PMF is far superior to that of the traditional SAR polarimetry. In terms of the APCM, the presence of $B\tau$ in the denominator on the right-hand side of (67) yields a difference of about $10\log_{10} B\tau$ (or, according to (63), more than $30dB$) compared to the traditional case; see (74) and (76). This is a very significant reduction of distortions.

If expressed via PPCM (see section 3.3.1), the difference turns out to be even bigger due to the sidelobe properties of W_1 and W_2; see (55b), (55c). Indeed, for the typical parameters from Table 1 we have $B\tau \gg 1$, $C_\tau = \mathcal{O}(1)$, and $|\eta| \lesssim 1$. Then, for $1 \lesssim |\xi| \ll B\tau$ the argument of $\cos(\cdot)$ and $\sin(\cdot)$ in (55) is small. Hence, using (48) and (55), we obtain $|W_1(\xi,\eta)| \approx \tau\left|\frac{2C_\tau}{B\tau}\eta\right||\sin\xi|$ and $|W_2(\xi,\eta)| \approx \tau\left|\frac{2C_\tau}{B\tau}\eta\right|^2|\xi\sin\xi|$. We see that for $|W_1|$, the leading local maxima with respect to ξ are essentially constant, while for $|W_2|$ the local maxima initially increase as $|\xi|$ increases. In either case, these maxima are nondecreasing and all of them, with the exception of the two closest to $\xi = 0$, are outside of the main lobe of $W_0(\xi)$. Hence, a considerable portion of the energy of W_1 and W_2 is contained in their sidelobes, which, however, do not contribute to the first integral in (61). As such, in the PMF case the numerator on the right-hand side of (64) will be many times bigger than the first integral in (61), while the difference between the denominator on the right-hand side of (64) and the second integral in (61) will be insignificant; see (57). This leads to a substantial difference between the PPCM and APCM for the PMF case. At the same time, for the functions $\tilde{W}_1$ and $\tilde{W}_2$ that pertain to the traditional polarimetry (see (71)), the percentage of energy in the sidelobes is much smaller, and the values of PPCM($\tilde{\mathbf{W}}$) and APCM($\tilde{\mathbf{W}}$) appear comparable, as can be seen in Figure 1.

In section SM1 of the supplementary materials, we outline how the current considerations are related to the single-polarization SAR imaging in the presence of FR, the case that we analyzed in our earlier work; see [10, Chapter 5].

4. Polarimetric imaging with a synthetic aperture. Transition to a realistic (i.e., three-dimensional) setup with the two-dimensional target (an area on the surface of the Earth) requires several principal modifications to the approach of section 3. First, the coordinates of the antenna, image, and target become three-dimensional, and we will denote these by $\boldsymbol{x}$, $\boldsymbol{y}$, and $\boldsymbol{z}$, respectively. Second, in order to obtain a cross-range (i.e., azimuthal) resolution, we will need to employ a synthetic array, which is a set of equally spaced transmit and receive times and locations of the antenna denoted by $(t_n, \boldsymbol{x}^n)$. Third, we will be using the full formula (2) for the FR angle; i.e., we will be taking into account the angle β between the direction of propagation and that of the magnetic field. Accounting for the angle β will give rise to the dFR in slow time, because the factor $R_{\boldsymbol{z}} \cos\beta$ in the expression for the FR angle may vary with the position of the antenna indexed by the slow time parameter n.

We assume the satellite trajectory to be a straight line parallel to the ground, at altitude H and horizontal distance L from the target (such that $R = \sqrt{H^2 + L^2}$ is the slant range), with the broadside direction of the antenna beam. The synthetic aperture (or synthetic array) is an interval of antenna locations $\boldsymbol{x}^n$ such that a given point of the target appears within the beam footprint for all n from this interval. The length of the synthetic aperture L_{SA} is equal to the size of the beam footprint in the direction along the trajectory (i.e., azimuth). The coordinate indices 1, 2, and 3 will correspond to the azimuth (along-track), ground range (cross-track), and vertical directions, respectively. Accordingly, for the image and target coordinates $\boldsymbol{y}$ and $\boldsymbol{z}$, we will assume $y_3 = z_3 = 0$, and for antenna positions,

$$\boldsymbol{x}^n = (x_1^n, -L, H) \quad \text{such that} \quad |x_1^n| \leqslant L_{\mathrm{SA}}/2. \tag{77}$$

One more important modification to be made when considering the realistic SAR imaging configuration is the variation of the electron number density with elevation. Formula (2) for the FR angle is derived for the propagation through a homogeneous plasma. However, this expression can easily be extended to describe the inhomogeneous propagation as well, for example, in a vertically stratified ionosphere: $N_{\mathrm{e}} = N_{\mathrm{e}}(h)$. It can be done provided that the wavelength is much shorter than the scale of variation of the electron number density, which is a constraint that almost universally holds. The key integral characteristic of a vertically stratified ionosphere is called the total electron content (TEC):

$$N_H \stackrel{\mathrm{def}}{=} \int_0^H N_{\mathrm{e}}(h)dh. \tag{78}$$

Ignoring the ray curvature (see [10, section 3.3] for details), for the propagation of a monochromatic wave we can write

$$\varphi_{\mathrm{F}} = -\frac{\Omega_{\mathrm{e}}\cos\beta}{2c\omega^2\cos\theta}\int_0^H \omega_{\mathrm{pe}}^2(h)\,dh = -\frac{R_{\boldsymbol{z}}}{2c}\frac{\bar{\omega}_{\mathrm{pe}}^2\Omega_{\mathrm{e}}\cos\beta}{\omega^2}, \tag{79}$$

where s is the distance along the ray (i.e, signal path), θ is the angle between the ray and $\mathbf{e}_3$, and

$$\bar{\omega}_{\mathrm{pe}}^2 = \frac{1}{H}\int_0^H \frac{4\pi e^2}{m_{\mathrm{e}}} N_{\mathrm{e}}(h)\,dh = \frac{4\pi e^2}{m_{\mathrm{e}}}\frac{N_H}{H}. \tag{80}$$

Hereafter, we will be using $\bar{\omega}_{\mathrm{pe}}^2$ instead of ω_{pe}^2 in the expressions for the FR angle; see (79). If necessary, the foregoing procedure can be extended to include spatial variations of the external magnetic field. We, however, consider the magnetic field of the Earth to be constant, which allows us to characterize the variation of the angle β between the magnetic field and the line of sight over the length of the synthetic array; see formula (82) below.

The ionospheric TEC (78) is a very important parameter that determines the level of distortions in transionospheric SAR. The actual value of the TEC depends on many factors including the geographic location, time of the day, and solar cycle. The value that we use in this work for performing quantitative estimates (see Table 1) is on the higher end of the range of physical measurements. For the parameters from Table 1, the maximum two-way FR angle is about 26 radians, which is more than four full revolutions.

4.1. PMF with synthetic aperture. We modify expressions (11) to describe a series of identical pulses emitted from multiple antenna positions indexed by n:

$$\begin{pmatrix} E_{\mathrm{H}}^{\mathrm{i}} \\ E_{\mathrm{V}}^{\mathrm{i}} \end{pmatrix}_{(\mathrm{H,V})}^{n} (t, \boldsymbol{x}^n) = \boldsymbol{E}_{(\mathrm{H,V})} A(t - t_n) e^{-i\omega_0(t-t_n)}. \tag{81}$$

Moreover, we consider the antenna at a standstill ($\boldsymbol{x}^n$ fixed) during the emission of the pulse. This assumption is a part of what's known as the start-stop approximation (see [10, Chapter 6] for more details).

It is convenient to immediately eliminate t_n by shifting the time variable in (81) by t_n. This is possible if no two reflected pulses can be received simultaneously at the same point, a condition we assume to be satisfied. Denote $\boldsymbol{R}_{\boldsymbol{z}}^n = \boldsymbol{z} - \boldsymbol{x}^n$, $R_{\boldsymbol{z}}^n = |\boldsymbol{R}_{\boldsymbol{z}}^n|$, $\mathbf{e}_{\boldsymbol{H}} = \boldsymbol{H}_0/|\boldsymbol{H}_0|$, where $\boldsymbol{H}_0$ is the external magnetic field. Using (79), we modify expression (19) to obtain the FR angle accumulated along the signal path between $\boldsymbol{x}^n$ and $\boldsymbol{z}$:

$$\varphi_{\mathrm{F}}^n(t, \boldsymbol{z}) = -\frac{(\boldsymbol{R}_{\boldsymbol{z}}^n, \mathbf{e}_{\boldsymbol{H}})}{2c}\frac{\bar{\omega}_{\mathrm{pe}}^2\Omega_{\mathrm{e}}}{\omega^2(t - 2R_{\boldsymbol{z}}^n/\bar{v}_{\mathrm{gr}}(\omega_0))}. \tag{82}$$

In formula (82), the instantaneous frequency $\omega = \omega(t)$ is still given by (13), i.e., $\omega(t) = \omega_0 + 2\alpha t$, and $\bar{v}_{\mathrm{gr}}$ is calculated according to (17) but with $\bar{\omega}_{\mathrm{pe}}^2$ of (80) substituted instead of ω_{pe}^2. Similarly to (19), $\varphi_{\mathrm{F}}^n(t, \boldsymbol{z})$ in (82) is one half of the two-way FR angle.

The derivation of the PMF formulation for the full-fledged SAR and the analysis of its accuracy follow the corresponding developments for single-pulse imaging in sections 3.1 and 3.3. The details are given in section SM2 of the supplementary materials, and the key points are as follows. Instead of expression (24) for the pulse scattered by a distributed target, we use

$$\mathbf{M}(t,\boldsymbol{x}^n) = \chi_{L_{\mathrm{SA}}}(x_1^n - z_1)\int e^{-i\omega_0 \mathrm{t}_{\mathrm{ph}}^n(t,\boldsymbol{z})} A(\mathrm{t}_{\mathrm{gr}}^n(t,\boldsymbol{z})) \mathbf{R}(\varphi_{\mathrm{F}}^n(t,\boldsymbol{z}))\cdot\mathbf{S}(\boldsymbol{z})\cdot\mathbf{R}(\varphi_{\mathrm{F}}^n(t,\boldsymbol{z}))\,d\boldsymbol{z}; \tag{83}$$

see also (SM2). As the target is two-dimensional, we have $d\boldsymbol{z} = dz_1dz_2$ (see [10, Chapter 7] for more details). Obviously, the phase and the rotation angle of a signal in (83) depend on both the slow time and the fast time. Hence, similarly to (25), we obtain the image by means of a filter that matches the phase and the rotation angle of the received signal in fast and slow time:

$$\mathbf{I}(\boldsymbol{y}) = \sum_n \chi_{L_{\mathrm{SA}}}(x_1^n - y_1)\int e^{i\omega_0 \mathrm{t}_{\mathrm{ph}}^n(t,\boldsymbol{y})}\overline{A(\mathrm{t}_{\mathrm{gr}}^n(t,\boldsymbol{y}))} \mathbf{R}(-\varphi_{\mathrm{F}}^n(t,\boldsymbol{y}))\cdot\mathbf{M}(t,\boldsymbol{x}^n)\cdot\mathbf{R}(-\varphi_{\mathrm{F}}^n(t,\boldsymbol{y}))\,dt; \tag{84}$$

see also (SM3). The imaging operator in the matrix form is similar to (35),

$$\boldsymbol{I}(\boldsymbol{y}) = \int \mathbf{W}(\boldsymbol{y},\boldsymbol{z})\cdot\boldsymbol{S}(\boldsymbol{z})\,d\boldsymbol{z}, \tag{85}$$

whereas the expression for $\mathbf{W}$ in (85) is obtained in (SM13),

$$\mathbf{W}(\boldsymbol{y},\boldsymbol{z}) = \mathbf{V}(\Delta\varphi_{\mathrm{F}})e^{i\Phi_0}W_{\mathrm{A}}(\xi_{\mathrm{A}})W_{\mathrm{R}}(\xi_{\mathrm{R}}), \tag{86}$$

where

$$\begin{aligned} W_{\mathrm{A}}(\xi_{\mathrm{A}}) &= \chi_{4\pi\mathfrak{F}}(\xi_{\mathrm{A}})N\left(1-\frac{|\xi_{\mathrm{A}}|}{2\pi\mathfrak{F}}\right)\operatorname{sinc}\left[\xi_{\mathrm{A}}\left(1-\frac{|\xi_{\mathrm{A}}|}{2\pi\mathfrak{F}}\right)\right],\\ W_{\mathrm{R}}(\xi_{\mathrm{R}}) &= \chi_{B\tau}(\xi_{\mathrm{R}})\tau\left(1-\frac{2|\xi_{\mathrm{R}}|}{B\tau}\right)\operatorname{sinc}\left[\xi_{\mathrm{R}}\left(1-\frac{2|\xi_{\mathrm{R}}|}{B\tau}\right)\right], \end{aligned}$$

$\Phi_0 = -2k_0(y_2 - z_2)\sin\theta$, $\xi_{\mathrm{A}} = k_0(y_1 - z_1)L_{\mathrm{SA}}/R$, $\xi_{\mathrm{R}} = B(y_2 - z_2)\sin\theta/\bar{v}_{\mathrm{gr}}(\omega_0)$, and $\mathfrak{F} = L_{\mathrm{SA}}^2/(R\lambda_0)$ is the Fresnel number computed for the aperture of size L_{SA}. In turn, the expression for $\Delta\varphi_{\mathrm{F}}$ that appears on the right-hand side of (86) is given by

$$\Delta\varphi_{\mathrm{F}} \approx \frac{1}{2\pi\mathfrak{F}}\eta_{\mathrm{A}}\xi_{\mathrm{A}} + \frac{2C_{\mathrm{R}}}{B\tau}\eta\xi_{\mathrm{R}}, \tag{87}$$

where

$$\eta_{\mathrm{A}} = -\varphi_{\mathrm{F}_0}\big(\mathbf{e}_{\boldsymbol{H}},\mathbf{e}_1\big)\frac{L_{\mathrm{SA}}}{R},\quad C_{\mathrm{R}} = \frac{(\mathbf{e}_{\boldsymbol{H}},\mathbf{e}_2)}{\sin\theta}\frac{\omega_0}{4B}\frac{\bar{v}_{\mathrm{gr}}\tau}{R} - \frac{(\boldsymbol{x}^{\mathrm{c}},\mathbf{e}_{\boldsymbol{H}})}{R} \tag{88}$$

(see (SM14) and (SM15)), and η is given by (52). Similarly to C_τ of (53), we have $C_{\mathrm{R}} = \mathcal{O}(1)$. In traditional PolSAR, the new parameter η_{A} will control the strength of the dFR effect in azimuth, as shown in section 4.2; see (90).

The overall estimate for APCM($\mathbf{W}$) for the full-fledged SAR case is given by formulae (SM16) and (SM21):

$$\mathrm{APCM}(\mathbf{W},\eta_{\mathrm{A}},\eta) \sim 10\log_{10}\left[\max\left(\frac{\eta_{\mathrm{A}}^2}{\mathfrak{F}},\frac{C_{\mathrm{R}}^2\eta^2}{B\tau},\frac{\eta_{\mathrm{A}}^4}{\mathfrak{F}},\frac{C_{\mathrm{R}}^4\eta^4}{B\tau}\right)\right]. \tag{89}$$

As η_{A} and η are comparable, and as long as $\mathfrak{F}$ and $B\tau$ are of the same order of magnitude (see Table 1), the resulting estimates of distortions are not significantly different from estimate (67) obtained for the single-pulse case. Thus, the key conclusion that the PMF guarantees a low level of distortions still holds.

4.2. Traditional PolSAR. In traditional PolSAR (see section 3.2), one first obtains the intermediate image $\mathbf{Y}(\boldsymbol{y})$ by applying the scalar part of the matched filter $e^{i\omega_0 \mathfrak{t}^n_{\rm ph}(t,\boldsymbol{y})}\overline{A(\mathfrak{t}^n_{\rm gr}(t,\boldsymbol{y}))}$ to each received channel as in formula (31). Then, similarly to (32), the intermediate image is converted into the final image using a constant FR angle $\varphi^*_{\rm F}$ that is independent of $\boldsymbol{y}$, t, or n (i.e., $\tilde{x}$). In the single-pulse (or one-dimensional) setting, the polarimetric distortions that characterize this approach are due to leaving out the dependence of the FR angle on the instantaneous frequency. In the full formulation with the synthetic aperture, we expect that this effect will have a comparable magnitude. Moreover, there is an additional source of polarimetric filter mismatches—the coefficient $\big(\boldsymbol{R}^n_{\boldsymbol{z}}, \mathbf{e}_{\boldsymbol{H}}\big)$ in the expression for the FR angle (82). Indeed, this factor depends on the antenna location x^n_1 and, consequently, varies with n in the azimuthal sum, while using a constant $\varphi^*_{\rm F}$ neglects this variation. In our subsequent analysis, we will extend the method of section 3.4 to account for these two sources of polarimetric distortions.

The dFR effect is always present in the actual scattered signal. Therefore, the imaging operator in the case of traditional PolSAR is represented by the same formulae (85), (86), but the argument of the matrix $\mathbf{V}(\Delta\varphi_{\rm F})$ of (37) is given by $\Delta\varphi_{\rm F}(t,\tilde{x},\boldsymbol{z}) = \varphi_{\rm F}(t,\tilde{x},\boldsymbol{z}) - \varphi^*_{\rm F}$, which is a two-dimensional generalization of formula (33). Similarly to the PMF case (see section 4.1), we will only summarize our findings hereafter, while the detailed analysis is presented in section SM3 of the supplementary materials. It can be shown that the expression for $\Delta\varphi_{\rm F}$ in the case of traditional PolSAR has the following form:

$$\Delta\varphi_{\rm F} = \eta_{\rm A} u_{\rm A} + \eta_{\rm R} u_{\rm R}, \tag{90}$$

where

$$\eta_{\rm A} = -\varphi_{{\rm F}_0}\big(\mathbf{e}_{\boldsymbol{H}}, \mathbf{e}_1\big)\frac{L_{\rm SA}}{R}, \quad \eta_{\rm R} = -\varphi_{{\rm F}_0}\frac{2B}{\omega_0}\frac{\big(\boldsymbol{z}^* - \boldsymbol{x}^{\rm c}, \mathbf{e}_{\boldsymbol{H}}\big)}{R} \tag{91}$$

and $u_{\rm A} = \tilde{x}/L_{\rm SA}$, $u_{\rm R} = \tilde{t}/\tau$ (cf. formula (70); see also (SM25) and (SM26)). Note that the expression for $\eta_{\rm A}$ coincides with that in (88), while the expression for $\eta_{\rm R}$ includes an additional factor, $\eta_{\rm R} = \eta\,\big(\boldsymbol{z}^* - \boldsymbol{x}^{\rm c}, \mathbf{e}_{\boldsymbol{H}}\big)/R$, as compared to η of (52). Clearly, this factor can be associated with $\cos\beta$; see (79) or (2). Unlike in the single-pulse case described by formula (70), in (90) we have two parameters, $\eta_{\rm A}$ and $\eta_{\rm R}$, that characterize the variation of the FR angle in slow and fast time $u_{\rm A}$ and $u_{\rm R}$, respectively, where $|u_{\rm A,R}| \leqslant 1/2$. With $\Delta\varphi_{\rm F}$ given by (90), the expression for the kernel of the imaging operator becomes

$$\tilde{\mathbf{W}}(\boldsymbol{y},\boldsymbol{z}) = N\tau e^{i\Phi_0}\int_{-1/2}^{1/2}\int_{-1/2}^{1/2} e^{-2i\xi_{\rm A}u_{\rm A} - 2i\xi_{\rm R}u_{\rm R}}\mathbf{V}(\eta_{\rm A}u_{\rm A} + \eta_{\rm R}u_{\rm R})\, du_{\rm A}\, du_{\rm R} \tag{92}$$

(see also (SM27)), where similarly to section 3.4, we use the tilde to distinguish between the case of traditional signal processing and that of the PMF. We will use the same notation for the individual entries of the matrix $\tilde{\mathbf{W}}$ as in formula (54) and section 3.4, while keeping in mind that $\tilde{W}_0$, $\tilde{W}_1$, and $\tilde{W}_2$ are now functions of $(\xi_{\rm A}, \eta_{\rm A}, \xi_{\rm R}, \eta_{\rm R})$, with the L_2 norms obtained by integration with respect to $\xi_{\rm A}$ and $\xi_{\rm R}$ (cf. formula (65)):

$$\|f\|_2^2\,(\eta_{\rm A},\eta_{\rm R}) \stackrel{\rm def}{=} \int_{-\infty}^{\infty}\int_{-\infty}^{\infty} |f(\xi_{\rm A},\eta_{\rm A},\xi_{\rm R},\eta_{\rm R})|^2 d\xi_{\rm A}\, d\xi_{\rm R}.$$

A direct computation leads to the following relations:

$$\frac{\|\tilde{W}_1\|_2^2(\eta_{\rm A},\eta_{\rm R})}{\|\tilde{W}_0\|_2^2(\eta_{\rm A},\eta_{\rm R})} = \frac{1-\operatorname{sinc}2\eta_{\rm A}\operatorname{sinc}2\eta_{\rm R}}{3+\operatorname{sinc}2\eta_{\rm A}\operatorname{sinc}2\eta_{\rm R}+4\operatorname{sinc}\eta_{\rm A}\operatorname{sinc}\eta_{\rm R}}, \tag{93a}$$

$$\frac{\|\tilde{W}_2\|_2^2(\eta_{\rm A},\eta_{\rm R})}{\|\tilde{W}_0\|_2^2(\eta_{\rm A},\eta_{\rm R})} = \frac{3+\operatorname{sinc}2\eta_{\rm A}\operatorname{sinc}2\eta_{\rm R}-4\operatorname{sinc}\eta_{\rm A}\operatorname{sinc}\eta_{\rm R}}{3+\operatorname{sinc}2\eta_{\rm A}\operatorname{sinc}2\eta_{\rm R}+4\operatorname{sinc}\eta_{\rm A}\operatorname{sinc}\eta_{\rm R}}; \tag{93b}$$

see formula (SM29) of the supplementary materials. According to (64) and (93), the resulting expression for the polarimetric contamination metric due to the kernel (92) is

$$\operatorname{APCM}(\tilde{\mathbf{W}},\eta_{\rm A},\eta_{\rm R}) = 10\log_{10}\frac{5-\operatorname{sinc}2\eta_{\rm A}\operatorname{sinc}2\eta_{\rm R}-4\operatorname{sinc}\eta_{\rm A}\operatorname{sinc}\eta_{\rm R}}{3+\operatorname{sinc}2\eta_{\rm A}\operatorname{sinc}2\eta_{\rm R}+4\operatorname{sinc}\eta_{\rm A}\operatorname{sinc}\eta_{\rm R}}. \tag{94}$$

The right-hand side of (94) is symmetric with respect to $\eta_{\rm A}$ and $\eta_{\rm R}$ and reduces to its single-pulse counterpart (74) if either of the arguments $\eta_{\rm A}$ or $\eta_{\rm R}$ turns into zero, which is expected. Accordingly, we expect that the polarimetric error will be significant if the absolute value of at least one of the dFR parameters, $|\eta_{\rm A}|$ or $|\eta_{\rm R}|$, is not small.

As $\max(|\eta_{\rm A}|,|\eta_{\rm R}|)\to 0$, we have the following asymptotic formulae for expressions (93):

$$\begin{aligned}
\frac{\|\tilde{W}_1\|_2^2(\eta_{\rm A},\eta_{\rm R})}{\|\tilde{W}_0\|_2^2(\eta_{\rm A},\eta_{\rm R})} &= \frac{\eta_{\rm A}^2+\eta_{\rm R}^2}{12} + \mathcal{O}\big((\eta_{\rm A}^2+\eta_{\rm R}^2)^2\big),\\
\frac{\|\tilde{W}_2\|_2^2(\eta_{\rm A},\eta_{\rm R})}{\|\tilde{W}_0\|_2^2(\eta_{\rm A},\eta_{\rm R})} &= \frac{\eta_{\rm A}^4+\eta_{\rm R}^4}{80} + \frac{\eta_{\rm A}^2\eta_{\rm R}^2}{24} + \mathcal{O}\big((\eta_{\rm A}^2+\eta_{\rm R}^2)^3\big).
\end{aligned}$$

Hence, according to (64), the leading term in the asymptotic expression for APCM is

$$\operatorname{APCM}(\tilde{\mathbf{W}},\eta_{\rm A},\eta_{\rm R}) \approx 10\log_{10}\frac{\eta_{\rm A}^2+\eta_{\rm R}^2}{6}. \tag{95}$$

Similarly to the single-pulse case (76), this leading term is contributed by $\tilde{W}_1$. Figure 2 (left panel) provides further comparison between $\tilde{W}_1$ and $\tilde{W}_2$.

In turn, the right panel of Figure 2 plots $\operatorname{APCM}(\tilde{\mathbf{W}})$ as a function of $\eta_{\rm R}$ for several constant values of $\eta_{\rm A}$. We can see a significant increase of distortions when either of the arguments exceeds 1. We also notice that the distortions are bigger than those characterized by the PMF expression (89) because the latter has large factors of $B\tau$ and $\mathfrak{F}$ in the denominators.

5. Discussion. We have proposed a novel signal processing procedure for polarimetric SAR that compensates for the effect of dFR. It can help improve the quality of spaceborne SAR images in the case where dFR is strong and the distortions it causes are substantial. If, however, the dFR effect is not too strong, the traditional PolSAR processing can still be used. It is therefore important to be able to determine the maximum admissible level of dFR for which the traditional polarimetric imaging is still acceptable. The answer to this question will, of course, depend on the maximum admissible level of polarimetric contamination, which, in turn, is determined by a specific application.

The most basic requirement for polarimetric fidelity is that the reflectivity in a certain channel should mostly contribute to the received signal in the same channel,

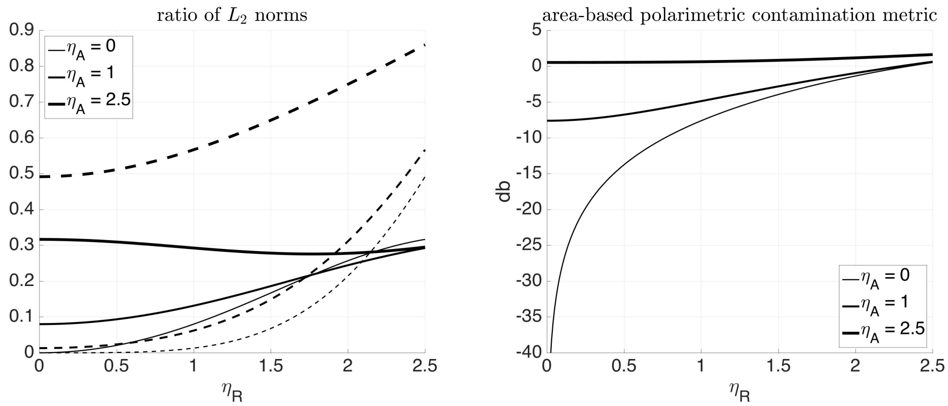

FIG. 2. *Left panel: Expressions* (93a) *(solid curves) and* (93b) *(dashed curves). Right panel: APCM*($\tilde{\mathbf{W}}$) *given by* (94). *The case* $\eta_A = 0$ *corresponds to the single-pulse setting of section* 3.4 *with* $\eta \equiv \eta_R$*; see the thick curves in Figure* 1.

i.e.,

$$\left\|\tilde{W}_1\right\|_2^2 \ll \left\|\tilde{W}_0\right\|_2^2, \quad \left\|\tilde{W}_2\right\|_2^2 \ll \left\|\tilde{W}_0\right\|_2^2, \tag{96a}$$

which implies that APCM($\tilde{\mathbf{W}}$) will be a negative number of sufficiently large magnitude.

A stronger condition comes from polarimetric applications. For natural surface types, the reflectivity in different channels may differ by up to $10\,dB$, i.e., 10 times in intensity (see, e.g., [6, Table I]). Consequently, the contamination of a channel by another channel with much stronger reflectivity will compromise the measurement of the former. Hence, the threshold given by (96a) should be reduced further:

$$\text{APCM}(\tilde{\mathbf{W}}) \ll -10\,dB. \tag{96b}$$

An even stronger limit on polarimetric contamination may be imposed by applications of polarimetric SAR interferometry (PolInSAR; see, e.g., [14, Chapter 9]), the most common probably being the measurement of the height and structure of the vegetation layer and determination of topography of the underlying terrain [17, 18]. The input data for PolInSAR processing is the coherence across the polarimetric channels between two or more SAR acquisitions. The resolution in the cross-slant direction (i.e., normal to the range and azimuth) is due to the elevation-dependent polarimetric phase of the interferogram, whereas the distinction between the ground and vegetation scattering is based on the assumption that the ground reflectivity is almost perfectly correlated, while the vegetation scattering is uncorrelated. Yet in the presence of dFR, the bare soil reflections will be superimposed on the polarimetric range sidelobes (e.g., on the leading extrema of $F_1(\xi_{\text{R}}, \eta_{\text{R}})$; see (72), and for more details, see (SM28b) in the supplementary materials) from much stronger vegetation scattering. For example, Table I from [6] shows that the bare soil reflectivity in one channel may be about 100 to 1000 times (20 to $30\,dB$) smaller than the reflectivity from vegetation in a different channel. This lowers the threshold of (96a), (96b) even further, to at least

$$\text{APCM}(\tilde{\mathbf{W}}) \ll -20\,dB. \tag{96c}$$

Given the various contamination thresholds (96a)–(96c), we can now assess the significance of the dFR effect for the parameters listed in Table 1. Replacing the dot products in (91) with the product of the corresponding absolute values, we obtain

$$\max|\eta_{\mathrm{A}}| \approx 0.65 \quad \text{and} \quad \max|\eta_{\mathrm{R}}| \approx 0.7. \tag{97}$$

The actual values of $|\eta_{\mathrm{A}}|$ and $|\eta_{\mathrm{R}}|$ depend on the direction of the magnetic field, and the foregoing maxima cannot be achieved simultaneously because the first one requires $\boldsymbol{H}_0 \parallel \mathbf{e}_1$, while the second one needs $\boldsymbol{H}_0 \perp \mathbf{e}_1$ (note that distortions are the smallest when $\boldsymbol{H}_0$ is normal to the slant plane: in this case $\varphi_{\mathrm{F}} \equiv 0$). Taking for definiteness $\eta_{\mathrm{A}} = 0$ and $\eta_{\mathrm{R}} = 0.7$, we obtain $\mathrm{APCM}(\tilde{\mathbf{W}}) \approx -11\,dB$ as the level of polarimetric contamination for traditional processing; see Figure 1. This level is acceptable for basic reflectivity measurements (96a) and for polarimetry (96b), but not for PolInSAR (96c). Switching to PMF processing will reduce the APCM by approximately $10\log_{10} B\tau$ or, according to (63), by more than $30\,dB$. Therefore, the PMF puts the estimates of polarimetric contamination safely below the thresholds for all of the aforementioned tasks (96a)–(96c). The reduction in PPCM can be expected to be even more substantial, as explained in section 3.5.

Obviously, the error levels depend on the system and ionospheric parameters. In particular, according to (91) and (38) there is a strong dependence of η_{A} and η_{R} on the carrier frequency: $\eta_{\mathrm{A}} \propto \omega_0^{-2}$ and $\eta_{\mathrm{R}} \propto \omega_0^{-3}$. Therefore, the susceptibility of a SAR system to dFR distortions decreases rapidly as the carrier frequency increases. Consider, for example, the radar parameters of the contemplated BIOMASS mission (see [13]),

$$\omega_0 = 435MHz, \quad B = 6MHz, \quad H = 670km, \quad \theta = 30^\circ,$$

and take the ionospheric parameters from Table 1 as before. Due mostly to higher carrier frequency ($435MHz$ versus $300MHz$), we obtain the value of $\max|\eta_{\mathrm{R}}| \approx 0.13$, which is about 5 times smaller than that in (97). Then, using the asymptotic formula (95) or (76) that pertains to $|\eta_{\mathrm{R}}| \ll 1$, we arrive at $\mathrm{APCM}(\tilde{\mathbf{W}}) \approx 10\log_{10}\left(3\cdot 10^{-3}\right) \approx -25\,dB$ for the case of traditional processing. The corresponding value of $\mathrm{PPCM}(\tilde{\mathbf{W}})$ will be about $1\,dB$ lower; see Figure 1. These levels of distortions are borderline. They may or may not be acceptable for PolInSAR requirements (see (96c)), even taking into account that they may become smaller for a lower TEC and/or more "favorable" direction of the magnetic field. Yet the use of the PMF processing for this SAR instrument would guarantee that the level of polarimetric contamination will always remain negligible regardless of a particular task or conditions of the ionosphere.

Note also that throughout the paper we have only used rectangular windows such as $\chi_\tau(t)$ of (12); see, e.g., the signal processing formulae (25) and (31). In practice, smoothing windows are often employed to suppress the sidelobes; see, e.g., [5, section 2.6]. This may, in particular, reduce the ISLR, as we have indicated in the discussion that follows (58). Given that in the case of the PMF processing the sidelobes of the off-diagonal entries of matrix $\mathbf{W}$ are wide (see section 3.5), it is reasonable to expect that windowing may significantly reduce the (already small) PMF errors. At the same time, in the case of traditional processing the off-diagonal entries of $\tilde{\mathbf{W}}$ mainly peak near the origin. Hence, no significant error reduction due to windowing should be expected. We leave this topic for a future study.

Yet another subject that may require additional attention is the development of even more subtle performance criteria, beyond the PPCM and APCM. These new criteria should be able to handle the delicate phenomena, such as the double intensity peaks that may appear in polarimetric images due to the odd/even nature of the various entries of the matrix PSF $\tilde{\mathbf{W}}$; see the discussion toward the end of section 3.4.

REFERENCES

[1] R. Bamler and M. Eineder, *Accuracy of differential shift estimation by correlation and split-bandwidth interferometry for wideband and delta-k SAR systems*, IEEE Geosci. Remote Sens. Lett., 2 (2005), pp. 151–155, https://doi.org/10.1109/LGRS.2004.843203.

[2] R. Brcic, A. Parizzi, M. Eineder, R. Bamler, and F. Meyer, *Estimation and compensation of ionospheric delay for SAR interferometry*, in Proceedings of IGARSS'10, Honolulu, HI, 2010, IEEE, pp. 2908–2911.

[3] V. N. Bringi and V. Chandrasekar, *Polarimetric Doppler Weather Radar: Principles and Applications*, Cambridge University Press, New York, 2001.

[4] M. Cheney and B. Borden, *Fundamentals of Radar Imaging*, CBMS-NSF Regional Conf. Ser. in Appl. Math. 79, SIAM, Philadelphia, 2009, https://doi.org/10.1137/1.9780898719291.

[5] I. G. Cumming and F. H. Wong, *Digital Processing of Synthetic Aperture Radar Data. Algorithms and Implementation*, Artech House, Boston, 2005.

[6] A. Freeman, *Calibration of linearly polarized polarimetric SAR data subject to Faraday rotation*, IEEE Trans. Geosci. Remote Sens., 42 (2004), pp. 1617–1624.

[7] A. Freeman and S. S. Saatchi, *On the detection of Faraday rotation in linearly polarized L-band SAR backscatter signatures*, IEEE Trans. Geosci. Remote Sens., 42 (2004), pp. 1607–1616.

[8] M. Gilman, E. Smith, and S. Tsynkov, *Reduction of ionospheric distortions for spaceborne synthetic aperture radar with the help of image registration*, Inverse Problems, 29 (2013), 054005, https://doi.org/10.1088/0266-5611/29/5/054005.

[9] M. Gilman, E. Smith, and S. Tsynkov, *Single-polarization SAR imaging in the presence of Faraday rotation*, Inverse Problems, 30 (2014), 075002, https://doi.org/10.1088/0266-5611/30/7/075002.

[10] M. Gilman, E. Smith, and S. Tsynkov, *Transionospheric synthetic aperture imaging*, Birkhäuser/Springer, Cham, Switzerland, 2017.

[11] V. L. Ginzburg, *The Propagation of Electromagnetic Waves in Plasmas*, Pergamon Press, Oxford, UK, 1964.

[12] R. A. Horn and C. R. Johnson, *Matrix Analysis*, Cambridge University Press, Cambridge, UK, 1985.

[13] T. Le Toan, S. Quegan, M. W. J. Davidson, H. Balzter, P. Paillou, K. Papathanassiou, S. Plummer, et al., *The BIOMASS mission: Mapping global forest biomass to better understand the terrestrial carbon cycle*, Remote Sens. Environ., 115 (2011), pp. 2850–2860.

[14] J.-S. Lee and E. Pottier, *Polarimetric Radar Imaging: From Basics to Applications*, CRC Press, Boca Raton, FL, 2009.

[15] F. J. Meyer, *Performance requirements for ionospheric correction of low-frequency SAR data*, IEEE Trans. Geosci. Remote Sens., 49 (2011), pp. 3694–3702, https://doi.org/10.1109/TGRS.2011.2146786.

[16] F. J. Meyer and J. B. Nicoll, *Prediction, detection, and correction of Faraday rotation in full-polarimetric L-band SAR data*, IEEE Trans. Geosci. Remote Sens., 46 (2008), pp. 3076–3086.

[17] A. Moreira, P. Prats-Iraola, M. Younis, G. Krieger, I. Hajnsek, and K. P. Papathanassiou, *A tutorial on synthetic aperture radar*, IEEE Geosci. Remote Sens. Mag., 1 (2013), pp. 6–43.

[18] K. P. Papathanassiou and S. R. Cloude, *Single-baseline polarimetric SAR interferometry*, IEEE Trans. Geosci. Remote Sens., 39 (2001), pp. 2352–2363.

[19] P. A. Rosen, S. Hensley, and C. Chen, *Measurement and mitigation of the ionosphere in L-band interferometric SAR data*, in Proceedings of the 2010 IEEE International Radar Conference, Arlington, VA, 2010, pp. 1459–1463.

[20] D. G. Swanson, *Plasma Waves*, 2nd ed., IOP Publishing, London, 2003.

[21] R. Torres, S. Lokas, H. L. Möller, M. Zink, and D. M. Simpson, *The TerraSAR-L mission and system*, in Proceedings of IGARSS'04, Vol. 7, IEEE, 2004, pp. 4519–4522.

[22] R. Touzi, F. J. Charbonneau, R. K. Hawkins, and P. W. Vachon, *Ship detection and characterization using polarimetric SAR*, Canad. J. Remote Sens., 30 (2004), pp. 552–559.

[23] K. Voccola, M. Cheney, and B. Yazici, *Polarimetric synthetic-aperture inversion for extended targets in clutter*, Inverse Problems, 29 (2013), 054003.

[24] P. A. Wright, S. Quegan, N. S. Wheadon, and C. D. Hall, *Faraday rotation effects on L-band spaceborne SAR data*, IEEE Trans. Geosci. Remote Sens., 41 (2003), pp. 2735–2744.

SUPPLEMENTARY MATERIALS: DIFFERENTIAL FARADAY ROTATION AND POLARIMETRIC SAR*

MIKHAIL GILMAN† AND SEMYON TSYNKOV‡

SM1. Single-polarization SAR imaging with differential Faraday rotation (dFR). Single-polarization SAR imaging is the imaging scenario where the SAR instrument has the capacity to send and receive only one given linear polarization. This limited capacity may be due to various engineering and technical constraints. Compared to the quad-pol imaging considered in this work, the analysis of single-polarization imaging in the presence of dFR (see [SM1, Chapter 5]) encounters additional difficulties.

In the quad-pol case, the transformation between the matrices $\mathbf{S}$ and $\mathbf{M}$, see formulae (20) and (22), is rendered by the orthogonal matrices $\mathbf{R}$ given by (3). Therefore, we have $\|\mathbf{S}\| = \|\mathbf{M}\|$, which means, in particular, that the aforementioned transformation may not cause any amplification of the error.

The single-polarization case is different though. We do not have four equations that would relate the entries of the matrices $\mathbf{M}$ and $\mathbf{S}$. Instead, we have one relation, say, for the HH channel, which one can derive from (35) and (37): $M_{\mathrm{HH}} \propto \big(S_{\mathrm{HH}} \cos^2 \varphi_{\mathrm{F}} + (S_{\mathrm{VH}} - S_{\mathrm{HV}}) \cos \varphi_{\mathrm{F}} \sin \varphi_{\mathrm{F}} - S_{\mathrm{VV}} \sin^2 \varphi_{\mathrm{F}}\big)$. The previous relation shall be combined with the standard assumption on target reflectivity in the case of single-polarization imaging, namely, that it is scalar and does not depend on the polarization (see [SM1, Section 5.3]): $S_{\mathrm{HV}} = S_{\mathrm{VH}} = 0$ and $S_{\mathrm{HH}} = S_{\mathrm{VV}}$. Then, denoting $S \stackrel{\text{def}}{=} S_{\mathrm{HH}} = S_{\mathrm{VV}}$, we obtain the relation $M_{\mathrm{HH}} \propto S(\cos^2 \varphi_{\mathrm{F}} - \sin^2 \varphi_{\mathrm{F}}) = S \cos 2\varphi_{\mathrm{F}}$, which is equivalent to the one used in [SM1, Chapter 5]. We thus see that the inverse problem of reconstructing S given M_{HH} appears poorly conditioned if $(2\varphi_{\mathrm{F}} \bmod \pi) \approx \pi/2$, i.e., if the two-way FR makes the received polarization (nearly) orthogonal to the emitted polarization. Poor conditioning means that small errors in M_{HH} may cause large errors in S.

Moreover, taking into account the variation of φ_{F} along the chirp also proves critical in the single-polarization case. Indeed, for a constant φ_{F}, we formally have no problem with single-polarization imaging as long as $\cos 2\varphi_{\mathrm{F}} \neq 0$. As, however, $\cos \varphi_{\mathrm{F}}$ varies with frequency (i.e., fast time) and z, this variation will manifest itself in the expressions for the signal received from a distributed target, see, e.g., (24). As shown in [SM1, Section 5.7], the case where $\cos 2\varphi_{\mathrm{F}}$ turns into zero, i.e., where the amplitude of the received signal may become zero, requires special care for SAR signal processing.

SM2. Formulations and estimates of distortions of polarimetric matched filtering in PolSAR. In this section, we provide a detailed treatment of the case summarized in Section 4.1 in the main text. We are assuming that the emitted field is a series of pulses, see (81), and the Faraday rotation angle for each pulse is

*Supplementary materials for SIAP MS#M114042.

Funding: This material is based upon work supported by the US Air Force Office of Scientific Research (AFOSR) under awards number FA9550-14-1-0218 and FA9550-17-1-0230.

†Corresponding author. Department of Mathematics, North Carolina State University, Box 8205, Raleigh, NC 27695 (mgilman@ncsu.edu, http://www4.ncsu.edu/~mgilman/).

‡Department of Mathematics, North Carolina State University, Box 8205, Raleigh, NC 27695, and Moscow Institute of Physics and Technology, Dolgoprudny, 141700, Russia (tsynkov@math.ncsu.edu, http://www4.ncsu.edu/~stsynkov/).

given by (82).

Replacing A_δ with plain A in (14) per the discussion that follows (43), we obtain the expression for the matrix $\mathbf{M}$ that represents the received signals due to the n-th pulse scattered by a point target at $\boldsymbol{z}$ [cf. formula (20)]:

$$\mathbf{M}(t,\boldsymbol{x}^n) = e^{-i\omega_0 \mathrm{t}^n_{\mathrm{ph}}(t,\boldsymbol{z})} A(\mathrm{t}^n_{\mathrm{gr}}(t,\boldsymbol{z}))\mathbf{R}(\varphi^n_{\mathrm{F}}(t,\boldsymbol{z}))\cdot \mathbf{S}\cdot \mathbf{R}(\varphi^n_{\mathrm{F}}(t,\boldsymbol{z})). \tag{SM1}$$

In formula (SM1), similarly to (19), $\mathrm{t}^n_{\mathrm{ph,gr}}(t,\boldsymbol{z}) \stackrel{\mathrm{def}}{=} t - 2R^n_{\boldsymbol{z}}/\bar{v}_{\mathrm{ph,gr}}(\omega_0)$. The scattered pulse in (SM1) is received at the same location $\boldsymbol{x}^n$ where the original pulse was emitted. In other words, the antenna is assumed motionless not only during the emission of the pulse, but also during its entire round-trip time to the target and back, as well as during its reception. This assumption constitutes the full-fledged start-stop approximation. The effect of this approximation on the final quality of the image is analyzed in [SM1, Chapter 6].

For the pulse scattered by a distributed target, we modify expression (24) as follows:

$$\begin{aligned}\mathbf{M}(t,\boldsymbol{x}^n) = \chi_{L_{\mathrm{SA}}}(x^n_1 - z_1)\int e^{-i\omega_0 \mathrm{t}^n_{\mathrm{ph}}(t,\boldsymbol{z})} A(\mathrm{t}^n_{\mathrm{gr}}(t,\boldsymbol{z}))&\\ \mathbf{R}(\varphi^n_{\mathrm{F}}(t,\boldsymbol{z}))\cdot \mathbf{S}(\boldsymbol{z})\cdot \mathbf{R}(\varphi^n_{\mathrm{F}}(t,\boldsymbol{z}))\,d\boldsymbol{z}&.\end{aligned} \tag{SM2}$$

As the target is two-dimensional, we have $d\boldsymbol{z} = dz_1dz_2$ (see [SM1, Chapter 7] for more detail). The factor $\chi_{L_{\mathrm{SA}}}(x^n_1 - z_1)$ specifies the size of the beam footprint in the azimuthal direction.

Obviously, the phase and rotation angle of a signal in (SM1) and (SM2) depend on both the slow time and fast time. Hence, similarly to (25), we obtain the image by means of a filter that matches the phase and rotation angle of the received signal in fast and slow time:

$$\begin{aligned}\mathbf{I}(\boldsymbol{y}) = \sum_n \chi_{L_{\mathrm{SA}}}(x^n_1 - y_1)\int e^{i\omega_0 \mathrm{t}^n_{\mathrm{ph}}(t,\boldsymbol{y})}\overline{A(\mathrm{t}^n_{\mathrm{gr}}(t,\boldsymbol{y}))}&\\ \mathbf{R}(-\varphi^n_{\mathrm{F}}(t,\boldsymbol{y}))\cdot \mathbf{M}(t,\boldsymbol{x}^n)\cdot \mathbf{R}(-\varphi^n_{\mathrm{F}}(t,\boldsymbol{y}))\,dt&.\end{aligned} \tag{SM3}$$

The factor $\chi_{L_{\mathrm{SA}}}(x^n_1 - y_1)$ defines the span of antenna locations $\boldsymbol{x}^n$ in the sum (SM3). It is the synthetic array of size L_{SA} centered about $x^n_1 = y_1$.

In our subsequent analysis, we will switch from the discrete "slow time" n to the continuous variable $\tilde{x}$ as follows:

$$n\Delta x_1 = n\frac{L_{\mathrm{SA}}}{N} = x^n_1 = x^{\mathrm{c}}_1 + \tilde{x}, \quad \text{where} \quad x^{\mathrm{c}}_1 = \frac{y_1+z_1}{2}, \quad |n| \leqslant \frac{N}{2}. \tag{SM4}$$

In formula (SM4), N is the number of pulses in the sum (SM3). The transition from n to $\tilde{x}$ is possible provided that Δx_1 is sufficiently small, see [SM1, Section 2.4.2]. Substituting (SM2) and (SM4) into (SM3), we obtain the imaging operator, which is convenient to represent in the matrix form [cf. formula (35)]:

$$\boldsymbol{I}(\boldsymbol{y}) = \int \mathbf{W}(\boldsymbol{y},\boldsymbol{z})\cdot \boldsymbol{S}(\boldsymbol{z})\,d\boldsymbol{z}. \tag{SM5}$$

Similarly to (36), the imaging kernel in formula (SM5) is given by

$$\begin{aligned}\text{(SM6)}\quad \mathbf{W}(\boldsymbol{y},\boldsymbol{z}) = \chi_{L_{\mathrm{SA}}}(y_1 - z_1)\frac{N}{L_{\mathrm{SA}}} \\ \int dt \int_{-L'_{\mathrm{SA}}/2}^{L'_{\mathrm{SA}}/2} d\tilde{x}\, e^{i\Phi(\boldsymbol{x},\boldsymbol{y},\boldsymbol{z})}\overline{A(\mathsf{t}_{\mathrm{gr}}(t,\boldsymbol{x},\boldsymbol{y}))}A(\mathsf{t}_{\mathrm{gr}}(t,\boldsymbol{x},\boldsymbol{z}))\mathbf{V}(\Delta\varphi_{\mathrm{F}}).\end{aligned}$$

where $L'_{\mathrm{SA}} = L_{\mathrm{SA}} - |y_1 - z_1|$,[1] the structure of the matrix $\mathbf{V}$ remains the same as in the single-pulse case, see (37), and

$$\text{(SM7)}\qquad \Phi(\boldsymbol{x},\boldsymbol{y},\boldsymbol{z}) = -2k_0(R_{\boldsymbol{y}} - R_{\boldsymbol{z}}), \quad \Delta\varphi_{\mathrm{F}} = \varphi_{\mathrm{F}}(t,\tilde{x},\boldsymbol{z}) - \varphi_{\mathrm{F}}(t,\tilde{x},\boldsymbol{y}).$$

In the multi-pulse setting, we call the kernel $\mathbf{W}(\boldsymbol{y},\boldsymbol{z})$ of the imaging operator (SM5) the generalized ambiguity function (GAF). Note that while the span of x_1^n in (SM3) is centered around y_1, the interval of $\tilde{x}$ in (SM6) is centered around zero, which is similar to having the integration interval in (42) symmetrized by means of a new integration variable $\tilde{t}$ defined in (43) (see [SM1, Chapter 2] for additional detail).

To calculate $\Delta\varphi_{\mathrm{F}}$, we will extend the procedure (39)–(41) to two dimensions. First, we replace (39) with $\Delta\varphi_{\mathrm{F}} \equiv \varphi_{\mathrm{F}}(t,\tilde{x},\boldsymbol{z}) - \varphi_{\mathrm{F}}(t,\tilde{x},\boldsymbol{y}) \approx \Big(\dfrac{\partial\varphi_{\mathrm{F}}}{\partial\boldsymbol{z}}(t,\tilde{x},\boldsymbol{z}), \boldsymbol{z} - \boldsymbol{y}\Big)$. Then, we introduce the coordinate form of $\boldsymbol{R_z}$ as $\boldsymbol{R_z} = \boldsymbol{z} - \boldsymbol{x} = (z_1, z_2, 0) - (x_1, -L, H) = (z_1 - x_1, z_2 + L, -H)$ and define

$$\text{(SM8)}\qquad \boldsymbol{s} = \frac{\partial|\boldsymbol{R_z}|}{\partial\boldsymbol{z}} \equiv \frac{\partial R_{\boldsymbol{z}}}{\partial\boldsymbol{z}} = \frac{1}{R_{\boldsymbol{z}}}(z_1 - x_1, z_2 + L, 0) \approx \Big(\frac{z_1 - x_1}{R}, \sin\theta, 0\Big),$$

where $R = \sqrt{H^2 + L^2}$ is the distance between the origin of the coordinate system and the antenna trajectory and $L = R\sin\theta$. From (13) we have:

$$\partial\omega(t - 2R_{\boldsymbol{z}}/\bar{v}_{\mathrm{gr}}(\omega_0))/\partial R_{\boldsymbol{z}} = -2B/\big(\bar{v}_{\mathrm{gr}}(\omega_0)\tau\big),$$

so that

$$\frac{\partial}{\partial\boldsymbol{z}}\frac{1}{\omega^2(t - 2R_{\boldsymbol{z}}/\bar{v}_{\mathrm{gr}}(\omega_0))} = \frac{\partial}{\partial R_{\boldsymbol{z}}}\frac{1}{\omega^2(t - 2R_{\boldsymbol{z}}/\bar{v}_{\mathrm{gr}}(\omega_0))}\frac{\partial R_{\boldsymbol{z}}}{\partial\boldsymbol{z}} = \frac{4B}{\omega^3\bar{v}_{\mathrm{gr}}(\omega_0)\tau}\boldsymbol{s}.$$

Using the previous relations, we obtain the following expression:

$$\text{(SM9)}\qquad \frac{\partial\varphi_{\mathrm{F}}}{\partial\boldsymbol{z}} = -\frac{\bar{\omega}_{\mathrm{pe}}^2\Omega_{\mathrm{e}}}{2c}\Big(\frac{1}{\omega^2}\mathbf{e}_{\boldsymbol{H}} + \big(\boldsymbol{R_z}, \mathbf{e}_{\boldsymbol{H}}\big)\frac{4B}{\omega^3\bar{v}_{\mathrm{gr}}(\omega_0)\tau}\boldsymbol{s}\Big)$$

which is a counterpart of the single-pulse formula (40). Therefore, similarly to (41), we obtain:

$$\text{(SM10)}\quad \Delta\varphi_{\mathrm{F}} \approx \Big(\frac{\partial\varphi_{\mathrm{F}}}{\partial\boldsymbol{z}}(0,0,\boldsymbol{0}), \boldsymbol{z} - \boldsymbol{y}\Big) = \varphi_{\mathrm{F}_0}\Big(\frac{(\mathbf{e}_{\boldsymbol{H}}, \boldsymbol{z} - \boldsymbol{y})}{R} + 4\frac{(-\boldsymbol{x}^{\mathrm{c}}, \mathbf{e}_{\boldsymbol{H}})}{R}\frac{B}{\omega_0}\frac{(\boldsymbol{s}^{\mathrm{c}}, \boldsymbol{z} - \boldsymbol{y})}{\bar{v}_{\mathrm{gr}}(\omega_0)\tau}\Big),$$

where $\varphi_{\mathrm{F}_0} = -\dfrac{R}{2c}\dfrac{\bar{\omega}_{\mathrm{pe}}^2\Omega_{\mathrm{e}}}{\omega_0^2}$ and $\boldsymbol{s}^{\mathrm{c}} = \dfrac{\partial|\boldsymbol{z} - \boldsymbol{x}^{\mathrm{c}}|}{\partial\boldsymbol{z}}\Big|_{\boldsymbol{z}=\boldsymbol{0}}$.

[1]Note that, similarly to (46), the integration interval for $\tilde{x}$ is determined by the intersection of the angular support of the signal scattered by the actual point target at $\boldsymbol{z}$ and that scattered by the assumed point target at $\boldsymbol{y}$, see [SM1, Section 2.3.2] for more detail.

In the rest of the analysis, we proceed similarly to Section 3.3. We show below that one can replace the GAF (SM6) with the following extension of the single-pulse formula (42):

$$\mathbf{W}(\boldsymbol{y},\boldsymbol{z}) = \mathbf{V}(\Delta\varphi_{\mathrm{F}})\chi_{L_{\mathrm{SA}}}(y_1 - z_1)\frac{N}{L_{\mathrm{SA}}} \int dt \int_{-L'_{\mathrm{SA}}/2}^{L'_{\mathrm{SA}}/2} d\tilde{x}\, e^{i\Phi(\boldsymbol{x},\boldsymbol{y},\boldsymbol{z})}\overline{A(\mathsf{t}_{\mathrm{gr}}(t,\boldsymbol{x},\boldsymbol{y}))}A(\mathsf{t}_{\mathrm{gr}}(t,\boldsymbol{x},\boldsymbol{z})), \tag{SM11}$$

where the argument of $\mathbf{V}$ is taken at $\tilde{t}=0$, $\tilde{x}=0$. Introducing the non-dimensional variables $u_{\mathrm{A}} = \tilde{x}/L_{\mathrm{SA}}$ and $u_{\mathrm{R}} = \tilde{t}/\tau$ and taking into account that $|\boldsymbol{z}|, |\boldsymbol{y}| \ll L_{\mathrm{SA}} \ll R$, we use the Pythagorean theorem and obtain $R_{\boldsymbol{y}} - R_{\boldsymbol{z}} \approx (y_2 - z_2)\sin\theta - (y_1 - z_1)\tilde{x}/R$. Hence, the integrand in (SM11) transforms into

$$e^{i\Phi(\boldsymbol{x},\boldsymbol{y},\boldsymbol{z})}\overline{A(\mathsf{t}_{\mathrm{gr}}(t,\boldsymbol{x},\boldsymbol{y}))}A(\mathsf{t}_{\mathrm{gr}}(t,\boldsymbol{x},\boldsymbol{z})) = e^{i(\Phi_0 - 2\xi_{\mathrm{A}}u_{\mathrm{A}} - 2\xi_{\mathrm{R}}u_{\mathrm{R}} - 2\xi_{\mathrm{A}}\frac{B}{\omega_0}u_{\mathrm{A}}u_{\mathrm{R}})}, \tag{SM12}$$

where $\Phi_0 = -2k_0(y_2 - z_2)\sin\theta$, $\xi_{\mathrm{A}} = k_0(y_1 - z_1)L_{\mathrm{SA}}/R$, $\xi_{\mathrm{R}} = B(y_2 - z_2)\sin\theta/\bar{v}_{\mathrm{gr}}(\omega_0)$. To justify the transition from (SM6) to (SM11), we use the same reasoning as led from (36) to (42). Namely, by evaluating the partial derivatives of $\Delta\varphi_{\mathrm{F}}$ given by (SM7), linearizing with respect to $(\boldsymbol{y}-\boldsymbol{z})$ [cf. formula (45)], and dropping the terms that contain the factor $\frac{L_{\mathrm{SA}}}{R} \ll 1$, we have: $\dfrac{\partial\Delta\varphi_{\mathrm{F}}}{\partial\tilde{t}} \approx \varphi_{\mathrm{F}_0}\dfrac{2B}{\omega_0\tau R}\Big(\mathbf{e}_{\boldsymbol{H}} + 6\dfrac{(-\boldsymbol{x}^{\mathrm{c}},\mathbf{e}_{\boldsymbol{H}})}{v_{\mathrm{gr}}(\omega_0)\tau}\dfrac{B}{\omega_0}\boldsymbol{s}^{\mathrm{c}}, \boldsymbol{y}-\boldsymbol{z}\Big)$ and $\dfrac{\partial\Delta\varphi_{\mathrm{F}}}{\partial\tilde{x}} \approx \varphi_{\mathrm{F}_0}\dfrac{4B}{\omega_0}\dfrac{1}{Rv_{\mathrm{gr}}(\omega_0)\tau}\Big(\big(\mathbf{e}_{\boldsymbol{H}},\mathbf{e}_1\big)\boldsymbol{s} + \dfrac{(-\boldsymbol{x}^{\mathrm{c}},\mathbf{e}_{\boldsymbol{H}})}{R}\mathbf{e}_1, \boldsymbol{y}-\boldsymbol{z}\Big)$. One can see that compared to the scalar term (SM12), the dependence of $\mathbf{V}(\Delta\varphi_{\mathrm{F}})$ of (37) on the integration variables t and $\tilde{x}$ is slow and can thus be disregarded, which yields (SM11).

As B/ω_0 is small, we will drop the last term in the exponent on the right-hand side of (SM12), which allows us to factorize the two-dimensional integral in (SM11) into a product of two one-dimensional integrals over ξ_{A} and ξ_{R} (it can be shown that the corresponding factorization error is insignificant). Each of the resulting two integrals is calculated similarly to (46). Thus, the GAF (SM11) becomes [cf. formula (47)]

$$\mathbf{W}(\boldsymbol{y},\boldsymbol{z}) = \mathbf{V}(\Delta\varphi_{\mathrm{F}})e^{i\Phi_0}W_{\mathrm{A}}(\xi_{\mathrm{A}})W_{\mathrm{R}}(\xi_{\mathrm{R}}), \tag{SM13}$$

where

$$\begin{aligned} W_{\mathrm{A}}(\xi_{\mathrm{A}}) &= \chi_{4\pi\mathfrak{F}}(\xi_{\mathrm{A}})N\Big(1 - \frac{|\xi_{\mathrm{A}}|}{2\pi\mathfrak{F}}\Big)\operatorname{sinc}\Big[\xi_{\mathrm{A}}\Big(1 - \frac{|\xi_{\mathrm{A}}|}{2\pi\mathfrak{F}}\Big)\Big], \\ W_{\mathrm{R}}(\xi_{\mathrm{R}}) &= \chi_{B\tau}(\xi_{\mathrm{R}})\tau\Big(1 - \frac{2|\xi_{\mathrm{R}}|}{B\tau}\Big)\operatorname{sinc}\Big[\xi_{\mathrm{R}}\Big(1 - \frac{2|\xi_{\mathrm{R}}|}{B\tau}\Big)\Big], \end{aligned}$$

and $\mathfrak{F} = L_{\mathrm{SA}}^2/(R\lambda_0)$ is the Fresnel number computed for the aperture of size L_{SA}. As SAR systems are specifically designed to operate in the near-field zone of the synthetic array, we have $\mathfrak{F} \gg 1$. In particular, for the values from Table 1, $\mathfrak{F} = 2.5\cdot 10^3$, which is numerically very close to another large dimensionless parameter, the compression ratio of the chirp $B\tau$.[2]

[2]In [SM1, Sections 2.4.6 and 2.6], we show that the linear variation of the local wavenumber along the synthetic array can be interpreted as an azimuthal chirp of length L_{SA}. Then, the ratio of the Fraunhofer length of the array $2L_{\mathrm{SA}}^2/\lambda_0$ to the distance R from the antenna to the target, which is large by design and equal to $2\mathfrak{F}$, can be thought of as the compression ratio in the azimuthal direction.

Noticing that the first component of $\boldsymbol{s}^{\mathrm{c}}$ is small, see (SM8), we rewrite formula (SM10) as follows:

$$\Delta\varphi_{\mathrm{F}} \approx \frac{1}{2\pi\mathfrak{F}}\eta_{\mathrm{A}}\xi_{\mathrm{A}} + \frac{2C_{\mathrm{R}}}{B\tau}\eta\xi_{\mathrm{R}}, \tag{SM14}$$

where

$$\eta_{\mathrm{A}} = -\varphi_{\mathrm{F}_0}\big(\mathbf{e}_{\boldsymbol{H}}, \mathbf{e}_1\big)\frac{L_{\mathrm{SA}}}{R}, \quad C_{\mathrm{R}} = \frac{\big(\mathbf{e}_{\boldsymbol{H}}, \mathbf{e}_2\big)}{\sin\theta}\frac{\omega_0}{4B}\frac{\bar{v}_{\mathrm{gr}}\tau}{R} - \frac{\big(\boldsymbol{x}^{\mathrm{c}}, \mathbf{e}_{\boldsymbol{H}}\big)}{R}, \tag{SM15}$$

and η is given by (52). Similarly to C_τ of (53), we have $C_{\mathrm{R}} = \mathcal{O}(1)$. Hereafter, we will also disregard the dependence of C_{R} on $\boldsymbol{z}$. In traditional PolSAR, the new parameter η_{A} will control the strength of the dFR effect in azimuth, as shown in Section 4.2, see (SM25). For the matrix $\mathbf{W}$ defined in (SM13), we will use the same notations of its entries as in (54), W_0, W_1, and W_2, but keep in mind that these entries will now be functions of ξ_{A}, η_{A}, ξ_{R}, and η.

In our subsequent analysis of image distortions, we will focus on the area-based metric that was first introduced in Section 3.3.2.[3] It is defined with the help of the L_2 norms of W_0, W_1, and W_2 [cf. formula (64)]:

$$\mathrm{APCM}(\mathbf{W}, \eta_{\mathrm{A}}, \eta) \stackrel{\mathrm{def}}{=} 10\log_{10}\frac{2\|W_1\|_2^2(\eta_{\mathrm{A}}, \eta) + \|W_2\|_2^2(\eta_{\mathrm{A}}, \eta)}{\|W_0\|_2^2(\eta_{\mathrm{A}}, \eta)}, \tag{SM16}$$

where for a function of four variables $f = f(\xi_{\mathrm{A}}, \eta_{\mathrm{A}}, \xi_{\mathrm{R}}, \eta)$, its L_2 norm is obtained by integration with respect ξ_{A} and ξ_{R} [cf. formula (65)]:

$$\|f\|_2^2\,(\eta_{\mathrm{A}}, \eta) \stackrel{\mathrm{def}}{=} \int_{-\infty}^{\infty}\int_{-\infty}^{\infty} |f(\xi_{\mathrm{A}}, \eta_{\mathrm{A}}, \xi_{\mathrm{R}}, \eta)|^2 d\xi_{\mathrm{A}}\, d\xi_{\mathrm{R}}.$$

Similarly to Section 3.3.2, in order to estimate the argument of $\log_{10}$ in (SM16), we will use $|\sin\xi| \leqslant |\xi|$, $|\cos\xi| \leqslant 1$; in particular, we write with the help of (SM14):

$$|\sin(\Delta\varphi_{\mathrm{F}})| \leqslant |\Delta\varphi_{\mathrm{F}}| \leqslant \left|\frac{\eta_{\mathrm{A}}\xi_{\mathrm{A}}}{2\pi\mathfrak{F}}\right| + \left|\frac{2C_{\mathrm{R}}\eta\xi_{\mathrm{R}}}{B\tau}\right|. \tag{SM17}$$

Then, taking into account (55b), (SM13), and (SM17), recalling that $\operatorname{sinc}\xi = \sin\xi/\xi$, and using the standard properties of the norm, we get:

$$\|W_1\|_2\,(\eta_{\mathrm{A}}, \eta) \leqslant \Big\|N\frac{\eta_{\mathrm{A}}}{2\pi\mathfrak{F}}\chi_{4\pi\mathfrak{F}}(\cdot)\Big\|_2 \cdot \Big\|W_{\mathrm{R}}(\cdot)\Big\|_2 + \Big\|W_{\mathrm{A}}(\cdot)\Big\|_2 \cdot \Big\|\tau\frac{2C_{\mathrm{R}}\eta}{B\tau}\chi_{B\tau}(\cdot)\Big\|_2,$$

where the norms on the right-hand side are one-dimensional as in (65). Combining the previous inequality with $\|W_{\mathrm{A}}(\cdot)\|_2 \approx N\sqrt{\pi}$ and $\|W_{\mathrm{R}}(\cdot)\|_2 \approx \tau\sqrt{\pi}$, we obtain $\|W_1\|_2\,(\eta_{\mathrm{A}}, \eta) \leqslant N\tau\Big(\frac{|\eta_{\mathrm{A}}|}{\sqrt{\mathfrak{F}}} + \frac{2\sqrt{\pi}|C_{\mathrm{R}}|\,|\eta|}{\sqrt{B\tau}}\Big)$. At the same time, an argument identical to that of Section 3.3.2 yields $\|W_0\|_2\,(\eta_{\mathrm{A}}, \eta) \approx \|W_{\mathrm{A}}(\cdot)\|_2 \cdot \|W_{\mathrm{R}}(\cdot)\|_2 \approx \pi N\tau$. Hence, we have:

$$\frac{\|W_1\|_2^2\,(\eta_{\mathrm{A}}, \eta)}{\|W_0\|_2^2\,(\eta_{\mathrm{A}}, \eta)} \sim \Big(\frac{2}{\sqrt{\mathfrak{F}}}|\eta_{\mathrm{A}}| + \frac{4\sqrt{\pi}}{\sqrt{B\tau}}|C_{\mathrm{R}}|\,|\eta|\Big)^2. \tag{SM18}$$

[3]It has been shown in Sections 3.3.1 and 3.3.2 that when the PMF is used, APCM yields a much higher level of distortions than PPCM. Hence, studying the APCM corresponds to the "worst case scenario."

As the factors in front of $|\eta_{\rm A}|$ and $|\eta|$ on the right-hand side of (SM18) are small, and $|\eta_{\rm A}|, |\eta| \lesssim 1$, the quotient on the left-hand side of (SM18) also appears small.

In turn, for $\|W_2\|_2$ we have:

$$\|W_2\|_2 \leqslant \Big\|N\xi_{\rm A}\Big(\frac{\eta_{\rm A}}{2\pi\mathfrak{F}}\Big)^2\chi_{4\pi\mathfrak{F}}(\cdot)\Big\|_2 \cdot \Big\|W_{\rm R}(\cdot)\Big\|_2 + 2\Big\|N\frac{\eta_{\rm A}}{2\pi\mathfrak{F}}\chi_{4\pi\mathfrak{F}}(\cdot)\Big\|_2 \cdot \Big\|\tau\frac{2C_{\rm R}\eta}{B\tau}\chi_{B\tau}(\cdot)\Big\|_2 + \Big\|W_{\rm A}(\cdot)\Big\|_2 \cdot \Big\|\tau\xi_{\rm R}\Big(\frac{2C_{\rm R}\eta}{B\tau}\Big)^2\chi_{B\tau}(\cdot)\Big\|_2.$$

This leads to $\|W_2\|_2 \leqslant N\tau\Big(\frac{\eta_{\rm A}^2}{\sqrt{3}\mathfrak{F}} + \frac{4}{\sqrt{\pi}}\frac{|C_{\rm R}\eta_{\rm A}\eta|}{\sqrt{\mathfrak{F}B\tau}} + \frac{2\sqrt{\pi}}{3}\frac{C_{\rm R}^2\eta^2}{\sqrt{B\tau}}\Big)$, and, eventually, to

$$\text{(SM19)} \qquad \frac{\|W_2\|_2^2\,(\eta_{\rm A},\eta)}{\|W_0\|_2^2\,(\eta_{\rm A},\eta)} \sim \Big(\frac{\eta_{\rm A}^2}{\sqrt{3}\mathfrak{F}} + \frac{4}{\sqrt{\pi}}\frac{|C_{\rm R}\eta_{\rm A}\eta|}{\sqrt{\mathfrak{F}B\tau}} + \frac{2\sqrt{\pi}}{3}\frac{C_{\rm R}^2\eta^2}{\sqrt{B\tau}}\Big)^2.$$

For $|\eta_{\rm A}| \ll 1$ and $|\eta| \ll 1$, this yields a much smaller quantity than (SM18). In general,

$$\text{(SM20)} \qquad \frac{\|W_2\|_2^2\,(\eta_{\rm A},\eta)}{\|W_0\|_2^2\,(\eta_{\rm A},\eta)} \sim \max\Big(\frac{\eta_{\rm A}^4}{\mathfrak{F}}, \frac{C_{\rm R}^4\eta^4}{B\tau}\Big),$$

which is comparable to (SM18) but still much smaller than one. The overall estimate for APCM($\mathbf{W}$) is obtained by substituting (SM18) and (SM19) into (SM16). In doing so, the dominant term under the logarithm is as follows:

$$\text{(SM21)} \qquad \max\Big(\frac{\eta_{\rm A}^2}{\mathfrak{F}}, \frac{C_{\rm R}^2\eta^2}{B\tau}, \frac{\eta_{\rm A}^4}{\mathfrak{F}}, \frac{C_{\rm R}^4\eta^4}{B\tau}\Big).$$

This expression is used in formula (89) in the main text of the article.

SM3. Polarimetric distortions of traditional PolSAR. In this section, we provide a detailed treatment of the estimation of distortions in the traditional PolSAR outlined in Section 4.2.

The imaging operator in the case of traditional PolSAR is represented by the same formulae (85)–(86) as the matched filter PolSAR, but the matrix $\mathbf{V}(\Delta\varphi_{\rm F})$ defined by (37) is supplied the argument $\Delta\varphi_{\rm F}(t,\tilde{x},\boldsymbol{z}) = \varphi_{\rm F}(t,\tilde{x},\boldsymbol{z}) - \varphi_{\rm F}^*$, cf. formula (33).

Unlike in the single-pulse case, for a fixed FR angle $\varphi_{\rm F}^*$ and antenna position $\boldsymbol{x}$ there is not one but an entire set of locations $\boldsymbol{z}^*$ that satisfy

$$\varphi_{\rm F}^* = -\frac{\bar{\omega}_{\rm pe}^2\Omega_{\rm e}}{2c}\frac{(\boldsymbol{z}^*-\boldsymbol{x}^{\rm c},\mathbf{e}_{\boldsymbol{H}})}{\omega_0^2}.$$

For definiteness, we take $z_1^* = x_1^{\rm c}$. Then [cf. formula (68)],

$$\text{(SM22)} \qquad \Delta\varphi_{\rm F}(t,\tilde{x},\boldsymbol{z}) = -\frac{\bar{\omega}_{\rm pe}^2\Omega_{\rm e}}{2c}\Big(\frac{(\boldsymbol{R}_{\boldsymbol{z}},\mathbf{e}_{\boldsymbol{H}})}{\omega^2(\mathrm{t}_{\rm gr}(t,z))} - \frac{(\boldsymbol{z}^*-\boldsymbol{x}^{\rm c},\mathbf{e}_{\boldsymbol{H}})}{\omega_0^2}\Big).$$

If we take $t^* = 2|\boldsymbol{z}^*-\boldsymbol{x}^{\rm c}|/\bar{v}_{\rm gr}$, then $\Delta\varphi_{\rm F}(t^*,0,\boldsymbol{z}^*) = 0$, and we can expand (SM22) to obtain

$$\Delta\varphi_{\rm F}(t,\tilde{x},\boldsymbol{z}) = \frac{\partial\Delta\varphi_{\rm F}}{\partial t}\cdot(t-t^*) + \frac{\partial\Delta\varphi_{\rm F}}{\partial\tilde{x}}\cdot\tilde{x} + \Big(\frac{\partial\Delta\varphi_{\rm F}}{\partial\boldsymbol{z}},\boldsymbol{z}-\boldsymbol{z}^*\Big),$$

where the partial derivatives are taken at $(t, \tilde{x}, \boldsymbol{z}) = (t^*, 0, \boldsymbol{z}^*)$. The derivative with respect to $\boldsymbol{z}$ is given by (SM9), and the other two derivatives are

$$\frac{\partial \Delta\varphi_{\mathrm{F}}}{\partial t}\Big|_{(t,\tilde{x},\boldsymbol{z})=(t^*,0,\boldsymbol{z}^*)} = \frac{\bar{\omega}_{\mathrm{pe}}^2 \Omega_{\mathrm{e}}}{2c} \frac{2B}{\omega_0} \frac{|\boldsymbol{z}^* - \boldsymbol{x}^{\mathrm{c}}|}{\tau}, \quad \frac{\partial \Delta\varphi_{\mathrm{F}}}{\partial \tilde{x}}\Big|_{(t,\tilde{x},\boldsymbol{z})=(t^*,0,\boldsymbol{z}^*)} = \frac{\bar{\omega}_{\mathrm{pe}}^2 \Omega_{\mathrm{e}}}{2c} \big(\mathbf{e}_{\boldsymbol{H}}, \mathbf{e}_1\big).$$

This yields:

$$\begin{aligned} \Delta\varphi_{\mathrm{F}} = -\frac{\bar{\omega}_{\mathrm{pe}}^2 \Omega_{\mathrm{e}}}{2c\omega_0^2} \Big[&\big(\mathbf{e}_{\boldsymbol{H}}, \boldsymbol{z} - \boldsymbol{z}^*\big) - \big(\mathbf{e}_{\boldsymbol{H}}, \mathbf{e}_1\big)\tilde{x} \\ &+ \frac{2B}{\omega_0} \big(\boldsymbol{z}^* - \boldsymbol{x}^{\mathrm{c}}, \mathbf{e}_{\boldsymbol{H}}\big) \Big(-\frac{t - t^*}{\tau} + 2\frac{\big(\boldsymbol{s}^*, \boldsymbol{z} - \boldsymbol{z}^*\big)}{\bar{v}_{\mathrm{gr}}(\omega_0)\tau} \Big) \Big], \end{aligned} \tag{SM23}$$

where $\boldsymbol{s}^* = \frac{\partial R_{\boldsymbol{z}}^{\mathrm{c}}}{\partial \boldsymbol{z}}\Big|_{\boldsymbol{z}=\boldsymbol{z}^*}$. Substituting $\tilde{t}$ of (43) into (SM23), using $l_{1,2} = y_{1,2} - z_{1,2}$, and keeping only the leading terms, we arrive at the following expression:

$$\begin{aligned} \Delta\varphi_{\mathrm{F}} = \varphi_{\mathrm{F}_0} \Big[&\underbrace{\frac{\big(\mathbf{e}_{\boldsymbol{H}}, \mathbf{e}_2\big)(z_2 - z_2^*)}{R}}_{\text{term 1}} - \underbrace{\Big(\frac{\big(\mathbf{e}_{\boldsymbol{H}}, \mathbf{e}_1\big) l_1}{2R} + \frac{2B}{\omega_0} \frac{\big(\boldsymbol{z}^* - \boldsymbol{x}^{\mathrm{c}}, \mathbf{e}_{\boldsymbol{H}}\big)}{R} \frac{l_2 \sin\theta}{\bar{v}_{\mathrm{gr}}(\omega_0)\tau} \Big)}_{\text{term 2}} \\ &- \underbrace{\Big(\big(\mathbf{e}_{\boldsymbol{H}}, \mathbf{e}_1\big) \frac{\tilde{x}}{R} + \frac{2B}{\omega_0} \frac{\big(\boldsymbol{z}^* - \boldsymbol{x}^{\mathrm{c}}, \mathbf{e}_{\boldsymbol{H}}\big)}{R} \frac{\tilde{t}}{\tau} \Big)}_{\text{term 3}} \Big]. \end{aligned} \tag{SM24}$$

Next, we will compare the right-hand side of (SM24) against its single-pulse counterpart (69).

Apart from the coefficients of order one, the most significant difference between (SM24) and (69) is the term proportional to $\tilde{x}$ on the last line of (SM24). This term will play the same role in the azimuthal integral as the term proportional to $\tilde{t}$ plays in the time integral, see Section 3.4. As for the terms 1 and 2 in (SM24), they are independent of the integration variables and appear of the same order of magnitude as their counterparts in (69). As the latter have been found insignificant in Section 3.4, we drop the terms 1 and 2 in (SM24) and present the resulting expression in the following form:

$$\Delta\varphi_{\mathrm{F}} = \eta_{\mathrm{A}} u_{\mathrm{A}} + \eta_{\mathrm{R}} u_{\mathrm{R}}, \tag{SM25}$$

where

$$\eta_{\mathrm{A}} = -\varphi_{\mathrm{F}_0} \big(\mathbf{e}_{\boldsymbol{H}}, \mathbf{e}_1\big) \frac{L_{\mathrm{SA}}}{R}, \quad \eta_{\mathrm{R}} = -\varphi_{\mathrm{F}_0} \frac{2B}{\omega_0} \frac{\big(\boldsymbol{z}^* - \boldsymbol{x}^{\mathrm{c}}, \mathbf{e}_{\boldsymbol{H}}\big)}{R}. \tag{SM26}$$

Compared to the PMF expression (SM10), the dependence of $\Delta\varphi_{\mathrm{F}}$ on the fast and slow time given by formula (SM25) cannot be replaced with the values taken at the centers of the corresponding intervals, $\tilde{t} = 0$ and $\tilde{x} = 0$.[4] Expressions (SM25)–(SM26) are reproduced in the main text as formulae (90)–(91).

With $\Delta\varphi_{\mathrm{F}}$ given by (90), formula (SM6) transforms into

$$\tilde{\mathbf{W}}(\boldsymbol{y}, \boldsymbol{z}) = N\tau e^{i\Phi_0} \int_{-1/2}^{1/2} \int_{-1/2}^{1/2} e^{-2i\xi_{\mathrm{A}} u_{\mathrm{A}} - 2i\xi_{\mathrm{R}} u_{\mathrm{R}}} \mathbf{V}(\eta_{\mathrm{A}} u_{\mathrm{A}} + \eta_{\mathrm{R}} u_{\mathrm{R}})\, du_{\mathrm{A}}\, du_{\mathrm{R}}, \tag{SM27}$$

[4] In the single-pulse case, this corresponds to the difference between (70) and (41).

where similarly to Section 3.4, we use the tilde to distinguish between the case of traditional signal processing and that of the PMF.

We will use the same notation for the individual entries of the matrix $\tilde{\mathbf{W}}$ as in formula (54) and Section 3.4, while keeping in mind that $\tilde{W}_0$, $\tilde{W}_1$, and $\tilde{W}_2$ are now functions of $(\xi_{\mathrm{A}}, \eta_{\mathrm{A}}, \xi_{\mathrm{R}}, \eta_{\mathrm{R}})$. To derive the expressions for $\tilde{W}_0$, $\tilde{W}_1$, and $\tilde{W}_2$, we use the double angle formulae for the entries of $\mathbf{V}(\eta_{\mathrm{A}} u_{\mathrm{A}} + \eta_{\mathrm{R}} u_{\mathrm{R}})$, see (37), followed by expansions into the products of trigonometric functions of $2\eta_{\mathrm{A}} u_{\mathrm{A}}$ and $2\eta_{\mathrm{R}} u_{\mathrm{R}}$. Then, the double integrals in (SM27) split into plain integrals over u_{A} and u_{R}, which yields [cf. formulae (71)–(72)]:

$$\tilde{W}_0(\xi_{\mathrm{A}}, \eta_{\mathrm{A}}, \xi_{\mathrm{R}}, \eta_{\mathrm{R}}) = \frac{N\tau e^{i\Phi_0}}{2}\big(\mathcal{F}(\xi_{\mathrm{A}})\mathcal{F}(\xi_{\mathrm{R}}) + F_0(\xi_{\mathrm{A}}, \eta_{\mathrm{A}})F_0(\xi_{\mathrm{R}}, \eta_{\mathrm{R}}) + F_1(\xi_{\mathrm{A}}, \eta_{\mathrm{A}})F_1(\xi_{\mathrm{R}}, \eta_{\mathrm{R}})\big), \tag{SM28a}$$

$$\tilde{W}_1(\xi_{\mathrm{A}}, \eta_{\mathrm{A}}, \xi_{\mathrm{R}}, \eta_{\mathrm{R}}) = \frac{N\tau e^{i\Phi_0}}{2i}\big(F_1(\xi_{\mathrm{A}}, \eta_{\mathrm{A}})F_0(\xi_{\mathrm{R}}, \eta_{\mathrm{R}}) + F_0(\xi_{\mathrm{A}}, \eta_{\mathrm{A}})F_1(\xi_{\mathrm{R}}, \eta_{\mathrm{R}})\big), \tag{SM28b}$$

$$\tilde{W}_2(\xi_{\mathrm{A}}, \eta_{\mathrm{A}}, \xi_{\mathrm{R}}, \eta_{\mathrm{R}}) = \frac{N\tau e^{i\Phi_0}}{2}\big(\mathcal{F}(\xi_{\mathrm{A}})\mathcal{F}(\xi_{\mathrm{R}}) - F_0(\xi_{\mathrm{A}}, \eta_{\mathrm{A}})F_0(\xi_{\mathrm{R}}, \eta_{\mathrm{R}}) - F_1(\xi_{\mathrm{A}}, \eta_{\mathrm{A}})F_1(\xi_{\mathrm{R}}, \eta_{\mathrm{R}})\big). \tag{SM28c}$$

Expressions (SM28) obtained for the full synthetic aperture (SA) formulation reduce to their single-pulse (1P) counterparts (71) if either of the dFR parameters η_{A} or η_{R} turns into zero, e.g.,

$$\tilde{W}_0^{\mathrm{SA}}(\xi_{\mathrm{A}}, 0, \xi_{\mathrm{R}}, \eta_{\mathrm{R}}) \equiv \tilde{W}_0^{\mathrm{1P}}(\xi_{\mathrm{R}}, \eta_{\mathrm{R}}) \quad \text{or} \quad \tilde{W}_0^{\mathrm{SA}}(\xi_{\mathrm{A}}, \eta_{\mathrm{A}}, \xi_{\mathrm{R}}, 0) \equiv \tilde{W}_0^{\mathrm{1P}}(\xi_{\mathrm{A}}, \eta_{\mathrm{A}}).$$

A direct computation of the L_2 norms of $\tilde{W}_0$, $\tilde{W}_1$, and $\tilde{W}_2$ leads to the following relations:

$$\frac{\big\|\tilde{W}_1\big\|_2^2(\eta_{\mathrm{A}}, \eta_{\mathrm{R}})}{\big\|\tilde{W}_0\big\|_2^2(\eta_{\mathrm{A}}, \eta_{\mathrm{R}})} = \frac{1 - \operatorname{sinc} 2\eta_{\mathrm{A}} \operatorname{sinc} 2\eta_{\mathrm{R}}}{3 + \operatorname{sinc} 2\eta_{\mathrm{A}} \operatorname{sinc} 2\eta_{\mathrm{R}} + 4 \operatorname{sinc} \eta_{\mathrm{A}} \operatorname{sinc} \eta_{\mathrm{R}}}, \tag{SM29a}$$

$$\frac{\big\|\tilde{W}_2\big\|_2^2(\eta_{\mathrm{A}}, \eta_{\mathrm{R}})}{\big\|\tilde{W}_0\big\|_2^2(\eta_{\mathrm{A}}, \eta_{\mathrm{R}})} = \frac{3 + \operatorname{sinc} 2\eta_{\mathrm{A}} \operatorname{sinc} 2\eta_{\mathrm{R}} - 4 \operatorname{sinc} \eta_{\mathrm{A}} \operatorname{sinc} \eta_{\mathrm{R}}}{3 + \operatorname{sinc} 2\eta_{\mathrm{A}} \operatorname{sinc} 2\eta_{\mathrm{R}} + 4 \operatorname{sinc} \eta_{\mathrm{A}} \operatorname{sinc} \eta_{\mathrm{R}}}. \tag{SM29b}$$

These expressions are reproduced in the main text as formulae (93a) and (93b), respectively.

REFERENCES

[SM1] M. Gilman, E. Smith, and S. Tsynkov, *Transionospheric synthetic aperture imaging*, Birkhäuser/Springer, Cham, Switzerland, 2017.